

SURI, Y., ISLAM, S.Z. and HOSSAIN, M. 2020. Proppant transport in dynamically propagating hydraulic fractures using CFD-XFEM approach. *International journal of rock mechanics and mining sciences* [online], 131, article ID 104356. Available from: <https://doi.org/10.1016/j.ijrmms.2020.104356>.

Proppant transport in dynamically propagating hydraulic fractures using CFD-XFEM approach.

SURI, Y., ISLAM, S.Z. and HOSSAIN, M.

2020



Proppant transport in dynamically propagating hydraulic fractures using CFD-XFEM approach

Yatin Suri, Sheikh Zahidul Islam*, and Mamdud Hossain
School of Engineering, Robert Gordon University, Aberdeen, AB10 7GJ, UK

*Corresponding author. Email: s.z.islam1@rgu.ac.uk

Phone: +44(0)1224 262319

Fax: +44(0)1224 262444

Abstract

Numerically modelling the fluid flow with proppant transport and fracture propagation together are one of the significant technical challenges in hydraulic fracturing of unconventional hydrocarbon reservoirs. The existing models either model the proppant transport physics in static predefined fracture geometry or account for the analytical models for defining the fracture propagation. Furthermore, the fluid leak-off effects are usually neglected in the hydrodynamics of proppant transport in the existing models. In the present paper, a dynamic and integrated numerical model is determined that uses computational fluid dynamics (CFD) technique to model the fluid flow with proppant transport and Extended finite element method (XFEM) to model the fracture propagation. The results of fracture propagation were validated with the real field results and analytical models, and the results of proppant transport are validated with the experimental results. The integrated model is then used to comprehensively investigate the hydrodynamical properties that directly affect the near-wellbore stress and proppant distribution inside the fracture. The model can accurately model the proppant physics and also propose a solution to a frequent challenge faced in the petroleum industry of fracture tip screen out. Thus, using the current model allows the petroleum engineers to design the hydraulic fracturing operation successfully, model simultaneously fracture propagation and fluid flow with proppant transport and gain confidence by tracking the distribution of proppants inside the fracture accurately.

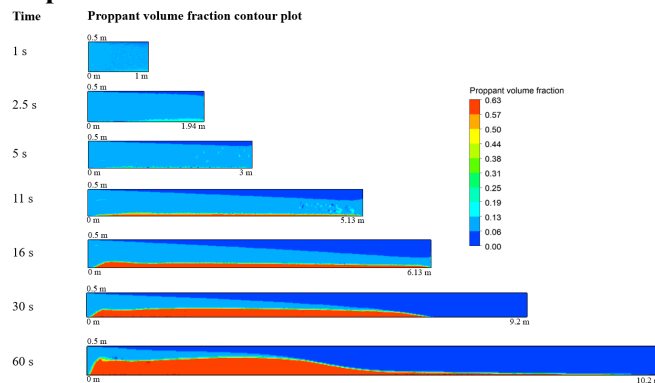
Keywords

Hydraulic fracturing, XFEM-based cohesive law, Computational Fluid Dynamics, Proppant transport; Fluid leak-off; Fracture propagation; Fracture tip screen-out

Highlights

- Proppant transport model with fluid leak-off and dynamic fracture propagation
- Fluid flow modelled using CFD-DEM hybrid model and propagation using XFEM model
- Results validated with real field data, analytical model and experimental study
- Effect of injection rate, fluid viscosity and leak-off rate investigated
- Investigated the parameters to mitigate fracture tip screen-out

Graphical abstract



1. Introduction

Hydraulic fracturing consists of four main processes: (1) the fracture initiation; (2) the fluid flow within the fracture; (3) the fracture growth or propagation; (4) the fluid leak-off from the fracture into the rock formation.¹ Linear elasticity is usually used to model fracture initiation; Lubrication theory is used to account for the fluid within the fracture; linear elastic fracture mechanics theory is adopted as the propagation law, and diffusion of fracturing fluid is used to account for fluid leak-off in the rock formation.²

The first theoretical mathematical models of hydraulic fracturing were developed in the 1950s. The two main models developed with the assumption of constant height were: the Khristianovic-Geertsma-de Klerk (KGD) model^{3,4} and the Perkins-Kern-Nordgren (PKN) model.^{5,6} KGD model is based on the assumption that width of the fracture is a function of length, the fracture is rectangular in shape and best suited for fractures whose height is much greater than its length^{3,4}, whereas PKN model assumes the width of fracture is a function of height; fracture is elliptical and is applicable when fracture length is much larger than the height.^{5,6} In addition, Yew and Weng⁷ explained that under uniform in-situ stress distribution, the hydraulic fracture is circular, and it can be characterised by KGD model. In contrast, under large and variable in-situ stress distribution, the hydraulic fracture becomes elongated and net wellbore pressure increases, this can be modelled by PKN model.

Simonson et al.⁸ developed Pseudo-3D (P3D) models based on PKN model to account for variation in height and examine the fracture propagation. The major difference between the P3D and the 2D models is the addition of a vertical in-situ stress profile and corresponding fluid flow component. P3D models can further be sub categorised into two main groups: Firstly, cell-based models proposed by Fung et al.⁹ who extended the work of Simonson et al.⁸ to multi-layer cases and divided fracture into several discrete and independent cells in the horizontal direction. The model is very reasonable in the central region of the fracture; however, it overestimates the magnitude of fluid pressure along the tip region of the fracture and cannot give an accurate description of pressure distribution in fracture. Furthermore, lumped models proposed by Cleary et al.¹⁰ which assumes a fractured front consists of two half ellipses combined. However, Johnson and Greenstreet¹¹ explained that these models cannot model excess leak off behaviour and cannot simulate fracturing with arbitrary shape. Thus, Planar3D (PL3D) models have been proposed by Advani et al.¹² that assumes the arbitrary shape of hydraulic fracture in a multilayered formation. In PL3D models, the fractures can be simulated using two approaches: fixed rectangular mesh¹³ using Green's function and moving triangular mesh¹². However, Carter et al.¹⁴ explained that PL3D model could not simulate out of plane fractures and deviated wellbore condition and thus, the fully 3D model is required to simulate the hydraulic fracturing process.

Barree and Conway¹⁵ developed a numerical simulation tool called GOHFER to improve the accuracy of the description of slurry transport and couple it with fracture propagation. However, for the proppant transport, the effect of concentration effects was included, and the effect of wall and inertia was neglected. Further, to couple the fracture propagation and fluid flow the analytical results of fracture width and pressure was used. Some of the simulation studies based on GOHFER¹⁶⁻¹⁸ also has the same limitation. Behr et al.¹⁹ and Shaoul et al.²⁰ further developed the work and proposed an approximate model integrating the fracture propagation and reservoir simulation, by importing the propped-fracture geometry in the commercial reservoir simulator. However, only the uniform proppant distribution is assumed in the analysis, and the dynamic effects of proppant transport and distribution were neglected in the modelling. Adachi et al.² developed a numerical simulation model for hydraulic fracturing. However, in their work, the proppant settling was assumed to be predominantly by gravity-based. In the absence of gravity, it was assumed that the fluid and proppant would transport with the same velocity. Further, to couple the fracture propagation and fluid flow the analytical results of fracture width and pressure was used. Frieauf²¹ in his research, developed a hydraulic fracturing model that

98 couple fluid flow and proppant transport. However, the fracture geometry was modelled using
99 analytical PKN model.

100
101 To simulate the 3D real-time fracturing process, Chen et al.¹ proposed a cohesive element
102 method. Unlike classical fracture mechanics, this model avoids the singularity problems in a
103 crack tip by using traction-separation law. It is implemented by the Finite Element Method
104 (FEM) and pre-assumes a fracture zone. In contrast, Zhang et al.²² suggested that this method
105 cannot predict the fracture orientation under complex stress condition, for example-
106 reorientation, because pre-installing cohesive elements predefine the fracture path. To improve
107 the method with less simulation cost, Zhou and Hou²³ introduced an approach to firstly,
108 categorise the elements into three groups: completely fractured, fracture front, unfractured
109 element. Secondly, weighted fluid pressure was calculated using fracture pressure of
110 completely fractured elements and the pore pressure of unfractured elements. Contrastingly,
111 this method estimated less accurate fracture profile, permeability and stress variation. To
112 simulate the interfacial attributes, Fu et al.²⁴, introduced a coupled model to capture nonlinear
113 interfacial interactions and model the permeability variation. In addition, Finite Volume
114 Method (FVM) together with FEM modelling, was used to simulate fluid flow reservoir
115 deformation. The main challenge in this method is that the crack could only grow along element
116 edges. Ribeiro²⁵ extended the work of Frieauf²¹ and used the adaptive remeshing technique,
117 but proposed the model only for the fully elastic medium and neglected the plastic deformations
118 in the medium. Recently, Wu²⁶, developed a hydraulic fracture propagation model from a
119 horizontal wellbore in a naturally fractured reservoir. The model integrated rock mechanics
120 using Displacement Discontinuity Method (DDM) with fluid mechanics using lubrication
121 theory. However, it does not incorporate proppant distribution in complex fracture networks
122 and assumes a constant height of fractures.

123
124 Some other methods to simulate hydraulic fracturing process include the eXtended Finite
125 Element Method (XFEM), and Discrete Element Method (DEM). Taleghani and Olson²⁷ used
126 XFEM to study fracture initiation, propagation and interactions between a growing hydraulic
127 fracture and the surrounding natural fracture. Keshavarzi and Mohammadi²⁸ extended this work
128 to study the effects of intersection angles between hydraulic fractures and natural fractures. The
129 Finite Element Method (FEM) is extensively used in fracture mechanics to model fracture
130 propagation. However, due to remeshing required at every time step, the FEM is
131 computationally expensive.²⁹ To overcome this shortcoming of FEM, an improved method
132 Extended Finite Element Method (XFEM) is proposed and used by many researchers
133 recently.^{27,30-33} In the XFEM, no re-meshing is required during fracture propagation, and
134 additional enriched degrees of freedom are introduced to model the fracture.³⁴⁻³⁶ In the current
135 research work, the XFEM was used to model the fracture propagation in unconventional
136 hydrocarbon reservoirs, and it is dynamically coupled with the fluid flow and proppant transport
137 model. Sousani et al.³⁷ modelled the hydraulic fracturing process using the discrete element
138 method (DEM) and studied the effect of fracture angle on stress and crack propagation. It was
139 shown that with the variation in fracture angle, it results in a change in the internal stress pattern
140 of the model. However, the capillary effects were neglected, and isotropic stress condition was
141 assumed, which become essential as fluid flows further away from the wellbore. Additionally,
142 to simulate the DEM to field scale, the simulation cost is very high.

143
144 In the existing coupled fluid flow and fracture models, the fluid flow and proppant transport are
145 usually modelled by two-component, interpenetrating continuum, meaning the flow governing
146 equations are specific to the mixture, which cannot provide the accurate description of the
147 particle physics in the slurry flow. Secondly, the effect of fracturing fluid leaking from the
148 fracture-matrix interface on proppant distribution is neglected. Moreover, lastly, in most of the
149 studies, the geometry of the fracture propagation is assumed from the analytical modelling
150 techniques. However, in the present paper, the proppant transport and fluid flow are modelled
151 solving the flow governing equation for both the phases individually and the proppant-fluid
152 interaction is explicitly modelled using Hybrid Model (CFD-DEM).³⁸ The model was then

153 integrated to couple the effect of dynamic fracture propagation with the fluid leak-off effects.
 154 The CFD, coupled with XFEM approach, offers the advantage of modelling the fracture
 155 propagation and investigate the accurate fluid flow and proppant concentration distribution,
 156 which may be challenging to obtain experimentally. The proposed three-dimensional integrated
 157 fluid flow, proppant transport and fracture propagation model can accurately model the fluid-
 158 proppant, proppant-proppant and fracture wall interactions with varying fluid, proppants and
 159 geomechanical parameters and fluid leak-off effects.

161 2. Methodology

162
 163 A fully coupled 3D hydraulic fracturing simulation involves the coupling of fracture mechanics
 164 that governs the fracture propagation with the fluid flow and proppant transport modelling that
 165 governs the pressure and velocity fields inside the fracture. A cohesive based XFEM technique
 166 is applied to calculate the rock stress, fracture initiation, propagation and rock deformation.
 167 Following that, a CFD method is applied to model the fluid flow and proppant transport
 168 numerically. The key underlying equation describing the cohesive based XFEM and finite
 169 volume based CFD-DEM is explained below.

171 2.1. Governing equations

172 The stress inside a poroelastic, isotropic and homogenous medium (Fig. 1) that is saturated with
 173 a single-phase fluid can be described by Eq. (1).^{39,40}

$$\begin{aligned} \nabla \cdot \boldsymbol{\sigma} &= \mathbf{0}, \text{ on } \Omega \\ \boldsymbol{\sigma} \cdot \mathbf{n} &= \mathbf{F}, \text{ on } \Gamma_F \\ \boldsymbol{\sigma} \cdot \mathbf{n}^- &= -\boldsymbol{\sigma} \cdot \mathbf{n}^+ = -pn^+ = pn^-, \text{ on } \Gamma_c \end{aligned} \quad (1)$$

174 where $\boldsymbol{\sigma}$ is the stress, \mathbf{F} is the external loading, p is the fluid pressure, and \mathbf{n} is the normal unit
 175 vector.

176 The strain-displacement equation and crack opening can be defined by Eq. (2), assuming small
 177 displacements and deformation,³⁹

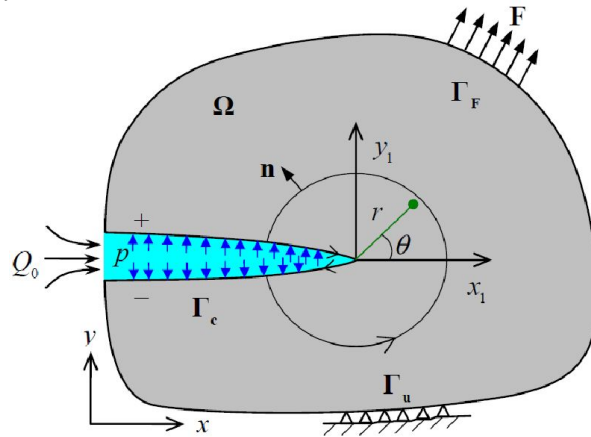
$$\begin{aligned} \boldsymbol{\varepsilon} &= (\nabla \mathbf{u} + (\nabla \mathbf{u})^T) / 2 \text{ on } \Omega \\ \mathbf{u} &= \mathbf{0} \text{ on } \Gamma_u \\ \mathbf{w} &= u^+ - u^- \text{ on } \Gamma_c \end{aligned} \quad (2)$$

178 where $\boldsymbol{\varepsilon}$ is the strain, \mathbf{w} is the crack opening, and \mathbf{u} is the displacement. The linear elastic
 179 constitutive law that governs the behaviour of the formation is described by Eq. (3)

$$\boldsymbol{\sigma} = \mathbf{D} : \boldsymbol{\varepsilon} \quad (3)$$

180 where \mathbf{D} is the Hooke's tensor.

181 According to the linear elastic fracture mechanics, the fracture propagation initiates when the
 182 mode I stress intensity factor K_I becomes equal to the critical stress intensity factor K_{IC} .



183
 184 Fig. 1. Hydraulic fracture in a porous rock formation³⁹

185 For an incompressible fracturing fluid, the mass conservation equation for the fluid flow in the
 186 fracture may be expressed as^{39,40}

$$\frac{\partial w}{\partial t} + \frac{\partial q}{\partial x} + c_L = 0 \quad (4)$$

187 where q is the fluid flux inside the fracture, c_L is the fluid leak-off rate from the fracture to the
 188 surrounding porous medium, and w is the fracture width. The fluid flow in the fracture is
 189 modelled using lubrication theory, given by Poiseuille's law.

$$q = -\frac{w^3}{12\mu} \frac{\partial p}{\partial x} \quad (5)$$

190 where $\frac{\partial p}{\partial x}$ is the pressure gradient, and μ is the dynamic fracturing fluid viscosity. Substituting
 191 Eq. (5) into Eq. (4) leads to the governing equation for the fluid flow within the fracture

$$\frac{\partial w}{\partial t} - \frac{\partial}{\partial x} \left(k \frac{\partial p}{\partial x} \right) + c_L = 0 \quad (6)$$

192 The general form of Eq. (6) can be written as

$$\dot{w} - \nabla T (\mathbf{k} \nabla p) + c_L = 0 \quad (7)$$

193 where $k = \frac{w^3}{12\mu}$ is the conductivity.

194 Eq. (7) can be solved using the following initial and boundary conditions in the hydraulic
 195 fracture,

$$\begin{aligned} q_{\text{inlet}} &= Q_0 \\ w_{\text{tip}} &= q_{\text{tip}} = 0 \end{aligned} \quad (8)$$

196 The equilibrium equation can be written in the weak form as^{39,40}

$$\int_{\Omega} \delta \boldsymbol{\varepsilon}^T \boldsymbol{\sigma} d\Omega - \int_{\Omega} \delta \mathbf{u}^T \mathbf{b} d\Omega - \int_{\Gamma_t} \delta \mathbf{u}^T \mathbf{t} d\Gamma - \left(\int_{\Gamma_c^+} \delta u_c^+ p_c^+ d\Gamma + \int_{\Gamma_c^-} \delta u_c^- p_c^- d\Gamma \right) = 0 \quad (9)$$

197 Where \mathbf{t} is the applied traction on the boundary Γ_t , \mathbf{b} is the body force, $\delta \mathbf{u}$ and $\delta \boldsymbol{\varepsilon}$ are the arbitrary
 198 virtual displacement and strain, related by $\delta \boldsymbol{\varepsilon} = \mathbf{S} \delta \mathbf{u}$ with \mathbf{S} as a strain operator.^{39,40}

199 The fluid pressure on the fracture surfaces and the fracture opening displacement is given by
 200 Eq. (10) and Eq. (11) respectively

$$\mathbf{p} = \mathbf{p}_c^+ = -\mathbf{p}_c^- = p \mathbf{n}_c = p \mathbf{n}_c^- = -p \mathbf{n}_c^+ \quad (10)$$

$$\mathbf{w} = \mathbf{n}_c^T \cdot (\mathbf{u}_c^+ - \mathbf{u}_c^-), \text{ or } \mathbf{w} = \mathbf{n}_c \cdot (\mathbf{u}_c^+ - \mathbf{u}_c^-) \quad (11)$$

201 Thus the equilibrium equation can be written in a simplified weak form as

$$\int_{\Omega} \delta \boldsymbol{\varepsilon}^T \boldsymbol{\sigma} d\Omega - \int_{\Omega} \delta \mathbf{u}^T \mathbf{b} d\Omega - \int_{\Gamma_t} \delta \mathbf{u}^T \mathbf{t} d\Gamma - \int_{\Gamma_c} \delta w^T \mathbf{p} d\Gamma = 0 \quad (12)$$

202 And the fluid flow governing equation within the fracture can be written in the weak form as

$$\int_{\Gamma_c} \delta p^T (\dot{w} - \nabla^T (\mathbf{k} \nabla p) + c_L) d\Gamma = 0 \quad (13)$$

203 Eq. (13) can further be simplified using integration by parts and the above boundary conditions
 204 as^{39,40}

$$\int_{\Gamma_c} \delta p^T \dot{w} d\Gamma + \int_{\Gamma_c} \nabla^T (\delta p) \mathbf{k} \nabla p d\Gamma + \int_{\Gamma_c} \delta p^T c_L d\Gamma = 0 \quad (14)$$

205 Using the standard (displacement) discretization method, the displacement vector \mathbf{u} , fluid
 206 pressure p , and fracture opening displacement \mathbf{w} can be approximated as

$$\begin{aligned} \mathbf{u} &\approx \hat{\mathbf{u}} = \sum_{i=1}^n N_i^u \mathbf{u}_i = N^u \tilde{\mathbf{u}}, \delta \mathbf{u} \approx N^u \delta \tilde{\mathbf{u}} \\ p &\approx \hat{p} = \sum_{i=1}^n N_i^p p_i = N^p \tilde{p}, \delta p \approx N^p \delta \tilde{p} \\ w &\approx \hat{w} = \sum_{i=1}^n N_i^w w_i = N^w \tilde{w}, \delta w \approx N^w \delta \tilde{w} \end{aligned} \quad (15)$$

207 where N_i^u , N_i^p and N_i^w are shape functions for nodal displacement (\mathbf{u}_i), fluid pressure (p_i), and
 208 crack opening respectively. Combining Eq. (15), Eq. (12), and Eq. (3) provides a system of
 209 algebraic equations for discrete fracture mechanics described by

$$K \tilde{\mathbf{u}} - Q \tilde{p} - f^u = 0 \quad (16)$$

210 Where

$$\begin{aligned} \mathbf{K} &= \int_{\Omega} B^T \mathbf{D} B d\Omega \\ f^u &= \int_{\Omega} (N^u)^T \mathbf{b} d\Omega + \int_{\Gamma_t} (N^u)^T \mathbf{t} d\Gamma \\ \mathbf{Q} &= \int_{\Gamma_c} (N^w)^T \mathbf{n} N^p d\Gamma \end{aligned} \quad (17)$$

211 Similarly, combining Eq. (15) and Eq. (14) provides a system of algebraic equations for discrete
212 fluid dynamics described by

$$C\tilde{u} - H\tilde{p} - f^p = 0 \quad (18)$$

213 Where

$$\begin{aligned} \mathbf{C} &= Q_T = \int_{\Gamma_c} (N^p)^T \mathbf{n}^T N^w d\Gamma \\ \mathbf{H} &= \int_{\Gamma_c} (\nabla N^p)^T \mathbf{k} \nabla N^p d\Gamma \\ f^p &= - \int_{\Gamma_c} (N^p)^T \mathbf{g} d\Gamma \end{aligned} \quad (19)$$

214 Thus, the discrete governing equations in the matrix form can be written as:

$$\begin{bmatrix} 0 & 0 \\ C & 0 \end{bmatrix} \begin{pmatrix} \tilde{u} \\ \tilde{p} \end{pmatrix} + \begin{bmatrix} K & -Q \\ 0 & H \end{bmatrix} \begin{pmatrix} \tilde{u} \\ \tilde{p} \end{pmatrix} = \begin{pmatrix} f^u \\ f^p \end{pmatrix} \quad (20)$$

215 The above equations form a finite element approach for a set of the coupled system of fracture
216 propagation and fluid flow in fracture. The XFEM is adopted to discretize and approximate the
217 displacement field u , as described in the following section.³⁹

218

219 *2.2. Extended finite element method (XFEM) approximation*

220

221 Belytschko and Black⁴¹ and Moes et al.³⁴ proposed the extended finite element in order to
222 provide a solution to the mesh-independent fracture propagation model. XFEM uses a partition
223 of unity technique from the study of Melenk and Babuska⁴² that extends the conventional FEM
224 approach and model any discontinuities with special enriched functions. XFEM has several
225 advantages over traditional techniques, including simulation of fracture propagation along
226 arbitrary paths independent of the mesh, additional degrees of freedom to model discontinuities
227 and simpler mesh refinement studies. Additionally, it improves the fracture tip solution by
228 avoiding re-meshing during the fracture propagation stage. Using the partition of unity
229 enrichment method, the displacement vector (u) can be described using Eq. (21).⁴³

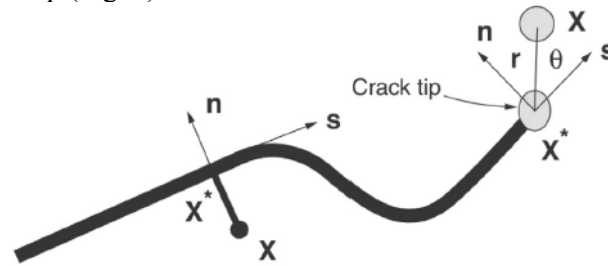
$$u = \sum_{i=1}^N N_i(x) \left[u_i + H(x) a_i + \sum_{j=1}^4 F_j(x) b_i^j \right] \quad (21)$$

230 The special enriched functions consist of two sub-functions: asymptotic element $F_j(x)$ and
231 discontinuous element $H(x)$. The asymptotic element aids in modelling the singularity near
232 fracture end and the discontinuous element represents the displacement jump near fracture
233 edges. $N_i(x)$ is the shape function with binary values depending upon the node location. The
234 nodal shape function has a value of one at the node where it is computed and zeroes at other
235 locations. u_i is the displacement that applies to all the nodes and linked to the continuous
236 element. a_i and b_i^j are the enriched degree of freedom at node and fracture end, respectively.
237 The discontinuous jump function and the asymptotic function can be defined by Eq. (22) and
238 Eq. (23) respectively.^{30,44}

$$H(x) = \begin{cases} 1 & \text{if } (x - x^*) \cdot n \geq 0 \\ -1 & \text{otherwise} \end{cases} \quad (22)$$

$$F_j(x) = \left[\sqrt{r} \sin \frac{\theta}{2}, \sqrt{r} \cos \frac{\theta}{2}, \sqrt{r} \sin \theta \sin \frac{\theta}{2}, \sqrt{r} \sin \theta \cos \frac{\theta}{2} \right] \quad (23)$$

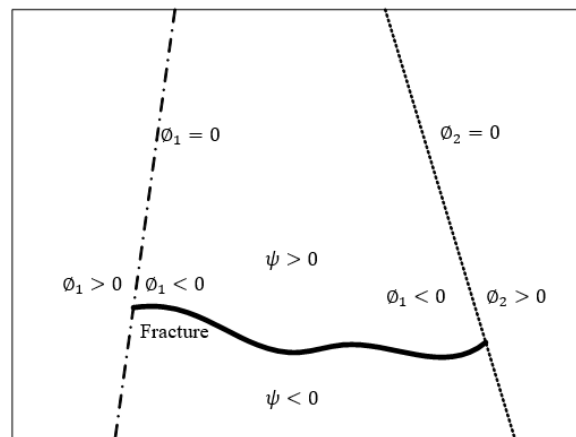
239 Where x and x^* are the sample point and the closest point on the crack from the sample point
 240 respectively, \mathbf{n} is the normal unit vector at x^* , r and θ are the polar coordinates with the origin
 241 located at the fracture tip (Fig. 2).



242
 243

Fig. 2. Illustration of the definition of special enriched functions⁴⁴

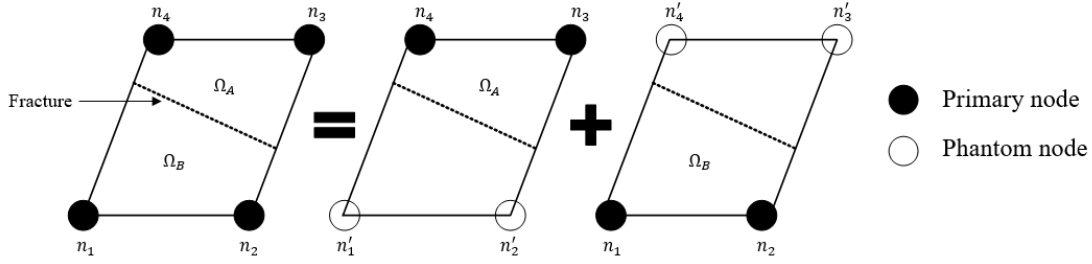
244 One of the significant advantages of the XFEM method over conventional fracture propagation
 245 modelling techniques is the description of the fracture. As stated earlier, XFEM aids in fracture
 246 propagation by avoiding re-meshing at each time step and thus is computationally attractive
 247 technique. Two important fracture propagation modelling techniques incorporated in the
 248 XFEM includes a level set method and phantom nodes. The level set method, proposed by
 249 Osher and Sethian⁴⁵, is used by XFEM to track the fracture interface and shape. The level set
 250 method assumes that two distance functions are required to describe fracture propagation.
 251 These distance functions are updated at each iterative time step and represented by ϕ and ψ .
 252 The first function, ϕ , refers to the fracture surface, whereas, ψ refers to the orthogonal fracture
 253 surface. The intersection of the surfaces defined by ϕ and ψ gives crack front. The XFEM
 254 fracture modelling mainly relies on the nodal data and is illustrated in Fig. 3.



255
 256

Fig. 3. Illustration of the fracture using the level set method (Modified from Chang⁴⁶)

257 Secondly, another important tool used to model the fracture discontinuity is using the phantom
 258 nodes.⁴⁷ When the formation mesh element is cut through by a fracture, then depending upon
 259 the fracture orientation, the cracked element can be split into two parts (Fig. 4). The phantom
 260 nodes can be assigned to the original nodes to model the discontinuity, and thus, the real nodes
 261 are no longer secured together and are free to separate apart. This method provides an effective
 262 approach for modelling crack growth in solids and provides promising results with mesh
 263 independent solution for a sufficiently refined mesh.^{44,48} As the fracture initiates, the fracture
 264 opening is governed by cohesive law until the fracture opening exceeds the cohesive strength
 265 of the element. Following that the phantom nodes and real nodes can separate independently.



266

267

Fig. 4. Illustration of phantom node method

268

2.3. Cohesive zone method

269

270

271

272

273

274

275

276

277

278

279

280

281

282

283

284

285

286

287

288

289

290

291

292

293

294

To model the fracture propagation in solid material or rocks requires different conditions or criterion to be defined that governs the advancement of the fracture tip. In fracture mechanics, the fracture can be analysed based on two fundamental approaches, namely energy criterion and stress intensity.⁴⁶ According to the energy criterion approach, fracture propagates when the energy available for fracture propagation overcomes the material resistance. The material resistance is commonly given by the critical energy release rate (G_c).⁴⁴ On the other hand, the stress intensity approach refers to a parameter known as stress intensity factor, commonly known as K_I that drives fracture propagation. For the linear elastic materials, both the approaches are equivalent. In Linear Elastic Fracture Mechanics (LEFM), the plastic deformation behaviour of the fracture tip region is neglected. Thus, LEFM is capable of modelling the fracture propagation for brittle mode when the K_I is greater than the critical stress intensity factor (K_{IC}). LEFM provides limitations to model the fracture propagation in quasi-brittle materials where the plastic deformation is significant. To overcome that a more robust modelling criterion is required that can model these non-linearities. Barenblatt⁴⁹ proposed a cohesive zone model that captures the plastic deformation non-linear behaviour. The traction–separation relationship is used to describe the constitutive behaviour of the cohesive zone that removes the limitation of singular stress at the fracture tip.⁵⁰ The cohesive zone model characterises the cohesive surfaces, which forms when the material elements are pulled apart. According to the traction–separation relationship, the traction value increases with the separation of cohesive surfaces until traction reaches a maximum value. Following that the traction value becomes zero, referring to full separation⁵¹ (Fig. 5). The detailed explanation of the traction–separation law with variables in Fig. 5 can be found in Högberg.⁵² The area enclosed in the traction–separation curve defines the energy required for separation, also known as critical fracture energy. The maximum nominal stress ratio criteria⁵³ are used in the present study that governs the fracture initiation and can be described by Eq. (25). When the stress ratios in Eq. (24) becomes unity; it marks the fracture initiation⁵⁴.

$$\text{Max} \left\{ \frac{\langle t_n \rangle}{t_n^0}, \frac{t_s}{t_s^0}, \frac{t_t}{t_t^0} \right\} = 1 \quad (24)$$

295

296

297

298

The fracture propagation is governed by the amount of degradation in rock stiffness. The amount of degradation is measured by a scalar variable D whose value range from zero (zero damage) to unity (full damage).³³ Due to the change in the value of degradation factor, D , the corresponding stress, t_n is also affected and can be described using the following expression:

$$t_n = \begin{cases} (1 - D)\bar{t}_n, & \bar{t}_n \geq 0 \\ \bar{t}_n, & \bar{t}_n < 0 \end{cases} \quad (25)$$

$$D = \frac{\delta_n^f(\delta_n^{\max} - \delta_n^0)}{\delta_n^{\max}(\delta_n^f - \delta_n^0)} \quad (26)$$

299

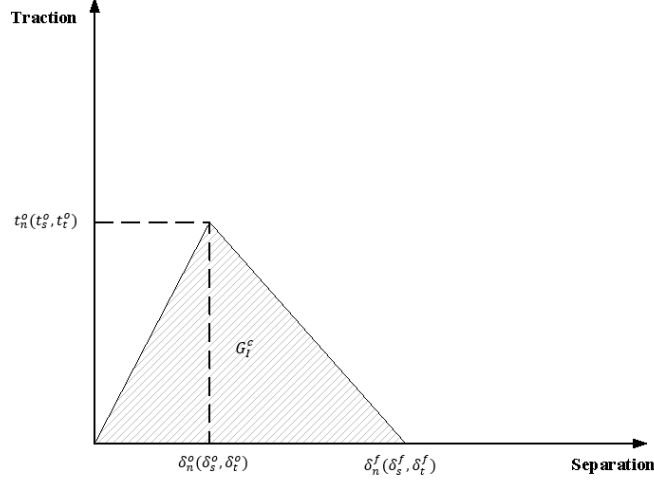
300

301

302

where δ_n^0 is the initial separation or displacement, δ_n^f is the separation at complete failure, δ_n^{\max} is the maximum separation, t_n is the stress in the normal direction, t_s is the stress in principle shear direction, and t_t is the stress in the second shear direction.

303 Conventionally in the oil and gas industry, the hydraulic fracture modelling is based on the
 304 LEFM and assumes only tensile forces for fracture propagation. However, in the formation with
 305 ductile properties, the shear forces can play a dominant role in fracture propagation. Depending
 306 upon the type of load applied, a fracture or crack can be initiated based on the following three
 307 modes. The first type of fracture is called mode I fracture, which is formed mainly due to tensile
 308 forces. The mode II fracture is due to the shear forces under sliding, and mode III fracture is
 309 due to the shear forces under tearing. Therefore, in the current study, a combined effect of
 310 different fracture modes is accounted to outline fracture initiation and propagation criteria.



311
 312 Fig. 5. Traction–separation relationship⁵⁵

313 In order to account for the mix mode fracture propagation, the criterion proposed by
 314 Benzeggagh and Kenane⁵⁶ was used. The fracture energy because of deformation, G^c can be
 315 described as

$$G^c = G_I^c + (G_{II}^c - G_I^c) \left(\frac{G_{\text{shear}}}{G_{\text{total}}} \right)^\eta \quad (27)$$

316 Where $G_I^c, G_{II}^c, G_{III}^c$ are the fracture energy due to traction-separation in normal, principle and
 317 second shear directions. $G_{\text{shear}} = G_{II}^c + G_{III}^c$, and $G_{\text{total}} = G_{\text{shear}} + G_I^c$. This study is based on
 318 the assumption that the results of fracture propagation due to traction separation law are the
 319 same in different modes because of the assumption of isotropic formation. Thus, the variables
 320 G_{II}^c and G_I^c are independent of η . The numerical model of fracture propagation proposed in the
 321 literature by researchers^{1,57,58} use the cohesive zone model, but they require the pre-defined
 322 path definition for crack growth. Thus, the XFEM and cohesive zone method can be combined
 323 to simulate the fracture propagation without defining the predefined paths and avoids the
 324 singularities around the fracture tip.⁵⁹

325 2.4. Governing equations of proppant transport and fluid flow in the fracture

326
 327 The multiphase flow of fluid with suspended proppants can be numerically modelled using
 328 mainly two methods- Eulerian-Granular method and Eulerian-Langrangian method (or Discrete
 329 Element method). In order to take advantage of both these methods, a hybrid model is used in
 330 the current study that tracks the trajectory of individual proppants using Eulerian-Langrangian
 331 approach with the fluid-proppant and inter-proppant interactions modelled using the kinetic
 332 theory of granular flow (KTGF) from Eulerian-Granular method. The equations describing the
 333 hybrid model for proppant transport used in the current study is explained in detail in our
 334 previous work.³⁸ However, the key governing equations are briefly described as follows.
 335 For an isothermal condition and incompressible fracturing fluid, the mass conservation equation
 336 is given by:

$$\rho_i \left(\frac{\partial}{\partial t} \alpha_i + \nabla \cdot \alpha_i \vec{v}_i \right) = S_m \quad (28)$$

337 Where ρ and v is the density and velocity respectively, α denotes the phase volume fraction,
 338 S_m denotes the mass source term and subscript i is the type of phase (liquid or solid)

$$\sum_i^n \alpha_i = 1 \quad (29)$$

339 The momentum conservation equation for the fluid phase is given by:

$$\frac{\partial}{\partial t} (\alpha_1 \rho_1 \vec{v}_1) + \nabla \cdot (\alpha_1 \rho_1 \vec{v}_1 \vec{v}_1) = -\alpha_1 \nabla p + \nabla \cdot \bar{\bar{\tau}}_1 + \alpha_1 \rho_1 \mathbf{g} + \vec{M}_{1s} + S_u \quad (30)$$

$$\bar{\bar{\tau}}_1 = \alpha_1 \mu_1 (\nabla \vec{v}_1 + \nabla \vec{v}_1^T) + \alpha_1 (\lambda_1 - \frac{2}{3} \mu_1) \nabla \cdot \vec{v}_1 \bar{\mathbf{I}} \quad (31)$$

340 Where \mathbf{g} refers to acceleration due to gravity, $\vec{M}_{1s} = \vec{M}_{s1}$ denotes the interfacial momentum
 341 exchange between the phases, S_u denotes the momentum source term, $\bar{\bar{\tau}}_1$ is the stress-strain
 342 tensor for the fluid described by Eq. (31), λ_1 and μ_1 denotes the bulk viscosity and dynamic
 343 viscosity of the fluid, respectively.

344 The proppant transport can be characterized by evaluating the force balance on the proppant
 345 using the Lagrangian reference frame. The proppant transport governing equations can be
 346 described using Newton's second law of motion by

$$m \frac{d\vec{v}_p}{dt} = \vec{F}_{\text{drag}} + \vec{F}_{\text{gravitation}} + \vec{F}_{\text{KTGF}} \quad (32)$$

$$\frac{d\mathbf{x}_p}{dt} = \vec{v}_p \quad (33)$$

347 The above equations can be re-written in the following form as

$$\frac{d\vec{v}_p}{dt} = \frac{\vec{v}_1 - \vec{v}_p}{\tau_r} + \frac{\mathbf{g}(\rho_p - \rho)}{\rho_p} + \vec{F}_{\text{KTGF}} \quad (34)$$

348 Where \vec{F}_{KTGF} , denotes the kinetic theory of granular flow (KTGF) interaction force due to
 349 particle-particle interaction given by-

$$\vec{F}_{\text{KTGF}} = -\frac{1}{\alpha_s \rho_s} \nabla \cdot \bar{\bar{\tau}}_s \quad (35)$$

350 Where $\bar{\bar{\tau}}_s$ is the proppant phase stress-strain tensor.

351 Eq. (34) defines the velocity of proppants and Eq. (33) defines the spatial location of the
 352 proppants. The variable τ_r in Eq. (34) is the relaxation time for particle defined by Eq. (36)

$$\tau_r = \frac{\rho_p d_p^2}{18\mu} \frac{24}{C_D \text{Re}} \quad (36)$$

353 $\frac{\vec{v}_1 - \vec{v}_p}{\tau_r}$ is the drag force per unit particle mass, \vec{v}_1 and \vec{v}_p are the fluid and particle velocity
 354 respectively, μ is the fluid viscosity, ρ and ρ_p are the fluid and particle density
 355 respectively, d_p is the particle diameter, and Re is the Reynolds number, defined as

$$\text{Re} = \frac{\rho d_p |\vec{v}_p - \vec{v}_1|}{\mu} \quad (37)$$

356 The drag force in Eq. (32) and the solid stress term for proppant transport in Eq. (35) are
 357 discussed in detail below.

358 2.4.1 Drag Force Modelling

359 The drag force is described by the Eq. (38). Numerous drag force models are available for
 360 multiphase flow modelling that differs in the definition of inter-phase momentum exchange
 361 coefficient, K_{ls} or K_{sl} .

$$\vec{F}_{\text{drag}} = K_{ls} (\vec{v}_1 - \vec{v}_s) \quad (38)$$

362 $\vec{v}_1 - \vec{v}_s$ is the relative velocity between the phases. Gidaspow⁶⁰ proposed a drag force model
 363 which provides the flexibility to use it for a wider application range based on the proppant
 364 volume fraction. Gidaspow drag model is used in the present study as described by Eq. (39):

$$K_{sl} = \begin{cases} 150 \frac{\alpha_s(1-\alpha_1)\mu_l}{\alpha_1 d_s^2} + 1.75 \frac{\rho_l \alpha_s |\vec{v}_s - \vec{v}_l|}{d_s} & \text{if } \alpha_s > 0.2 \\ \frac{3}{4} C_D \frac{\rho_l \alpha_s \alpha_1 |\vec{v}_s - \vec{v}_l|}{d_s} \alpha_1^{-2.65} & \text{if } \alpha_s < 0.2 \end{cases} \quad (39)$$

365 Where d_s is the proppant diameter and C_D is the drag coefficient calculated by Eq. (40).

$$C_D = \begin{cases} \frac{24}{\alpha_1 \text{Re}_s} [1 + 0.15(\alpha_1 \text{Re}_s)^{0.687}] & \text{if } \alpha_1 \text{Re}_s < 1000 \\ 0.44 & \text{if } \alpha_1 \text{Re}_s > 1000 \end{cases} \quad (40)$$

366 Where Re_s refers to the Reynolds number of the proppant phase and calculated by:

$$\text{Re}_s = \frac{\rho_l d_s |\vec{v}_s - \vec{v}_l|}{\mu_l} \quad (41)$$

367 2.4.2 Stresses Model for the proppant phase

368 Savage and Jeffrey⁶¹ described that the solid stress for the proppant phase, $\bar{\tau}_s$ (in Eq. (35)) is
369 based on the KTGF model as expressed in Eq. (42)

$$\bar{\tau}_s = (-P_s + \lambda_s \nabla \cdot \mu_s) \mathbf{I} + \mu_s \left\{ [\nabla \mu_s + (\nabla \mu_s)^T] - \frac{2}{3} (\nabla \cdot \mu_s) \bar{\mathbf{I}} \right\} \quad (42)$$

370 Where λ_s and μ_s refer to the bulk viscosity and dynamic viscosity of the granular phase
371 respectively and $\bar{\mathbf{I}}$ is the unit tensor.

372 2.4.3 Granular Temperature

373 In KTGF, the velocity fluctuation of the granular phase can be modelled using the granular
374 temperature as a function of specific kinetic energy. The granular temperature, Θ_s , can be
375 expressed in Eq. (43).

$$\Theta_s = \frac{1}{3} \langle v_s^2 \rangle \quad (43)$$

376 Where v_s is the velocity fluctuation of proppants.

377 The granular energy transport equation can be described by Eq. (44). The granular temperature
378 can be calculated by solving the granular energy transport equation. Alternatively, the granular
379 temperature can be calculated by using an algebraic expression. Van Wachem et al.⁶² simplified
380 the granular energy transport equation and proposed an algebraic expression to evaluate the
381 granular temperature by assuming the steady-state condition and neglecting the convection
382 and diffusion terms, given by Eq. (45).³⁸

$$\frac{3}{2} \left[\frac{\partial}{\partial t} (\alpha_s \rho_s \Theta_s) + \nabla \cdot (\alpha_s \rho_s \Theta_s) \vec{v}_s \right] = (-P_s \bar{\mathbf{I}} + \bar{\tau}_s) : \nabla \vec{v}_s + \nabla \cdot (k_{\Theta_s} \nabla \Theta_s) - \gamma_{\Theta_s} \Phi_{ls} \quad (44)$$

$$0 = (-P_s \bar{\mathbf{I}} + \bar{\tau}_s) : \nabla \vec{v}_s - \gamma_{\Theta_s} \Phi_{ls} \quad (45)$$

383 Where γ_{Θ_s} is the granular energy dissipation rate due to an inelastic collision, Φ_{ls} refers to the
384 interphase granular energy transfer, α_s is the volume fraction of proppants, k_{Θ_s} is the diffusion
385 coefficient, and P_s is the solid phase pressure that is a function of the normal force due to
386 particles motion. Lun et al.⁶³ proposed a correlation for P_s given by Eq. (46) and the probability
387 function of inter-particle interaction, $g_{0,ss}$, described by Eq. (47).

$$P_s = \rho_s \alpha_s \Theta_s + 2 \rho_s \alpha_s^2 \Theta_s (1 + e_{ss}) g_{0,ss} \quad (46)$$

$$g_{0,ss} = \left[1 - \left(\frac{\alpha_s}{\alpha_{s,max}} \right)^{\frac{1}{3}} \right]^{-1} \quad (47)$$

388 where e_{ss} is the restitution coefficient due to particles collision. $e_{ss} = 0.9$ representing inelastic
389 collision is used in the present study.³⁸ $\alpha_{s,max}$ is the maximum packing limit for the particles. In
390 the present study, a maximum packing limit of 0.63 is used.³⁸

391

392 2.4.4 Granular Shear Viscosity

393 The granular shear viscosity used in the solid stress model (Eq. (42)) is a combination of the
394 kinetic viscosity, collisional viscosity and frictional viscosity, as described in Eq. (48)

$$\mu_s = \mu_{s,kin} + \mu_{s,col} + \mu_{s,fr} \quad (48)$$

395 Gidaspow et al.⁶⁵, Gidaspow⁶⁰ and Johnson and Jackson⁶⁶ models given in Eqs. (49), (50) and
 396 (51) respectively are used to calculate the three components of viscosity.³⁸

$$\mu_{s,kin} = \frac{10\rho_s d_s \sqrt{\Theta_s \pi}}{96 \alpha_s g_{0,ss} (1 + e_{ss})} \left[1 + \frac{4}{5} \alpha_s g_{0,ss} (1 + e_{ss}) \right]^2 \quad (49)$$

$$\mu_{s,col} = \frac{4}{5} \alpha_s \rho_s d_s g_{0,ss} (1 + e_{ss}) \left(\frac{\Theta_s}{\pi} \right)^{\frac{1}{2}} \quad (50)$$

$$\mu_{s,fr} = P_{sf} \sin \theta \quad (51)$$

$$P_{sf} = F_r \frac{(\alpha_s - \alpha_{s,min})^n}{(\alpha_{s,max} - \alpha_s)^p} \quad (52)$$

397 Where $\mu_{s,kin}$, $\mu_{s,col}$, and $\mu_{s,fr}$ are the kinetic, collisional, and frictional viscosity, respectively. θ
 398 and P_{sf} are the friction angle and friction pressure, respectively. $\theta = 30^\circ$ is used in the present
 399 study.³⁸ Johnson and Jackson⁶⁶ proposed a model to calculate friction pressure given in Eq.
 400 (52). F_r , n , and p are constants and equals 0.1 α_s , 2, and 5, respectively. $\alpha_{s,max}$ is the maximum
 401 volume fraction of proppant, also known as packing limit. $\alpha_{s,max} = 0.63$ is used in the present
 402 study. $\alpha_{s,min}$ refers to the minimum volume fraction when the friction becomes dominant
 403 (approximately 0.6).³⁸

404 2.5. Coupling between XFEM and CFD

405
 406 An explicit coupling simulation approach is used in the present study to integrate the XFEM
 407 based fracture propagation model with the CFD-DEM based fluid flow and proppant transport
 408 model. Important elements in the current numerical model include the following:

- 409 • An XFEM geomechanics solver based on cohesive traction law that models the fracture
 410 propagation based on fracture mechanics, geomechanical stress and reservoir
 411 properties.
- 412 • A CFD based solver for modelling proppant transport inside the fracture with fluid
 413 leaking off from the fracture-matrix interface.

414 Fig. 6 shows the workflow that was followed in the current numerical model. Firstly, the XFEM
 415 model was configured using the available real field reservoir and geomechanical data, as shown
 416 in Table 1. Then the simulation run was performed to model the fracture propagation and get
 417 the fracture geometry which will then be used as a computational domain for the proppant
 418 transport and fluid flow in the CFD solver. The computational domain was discretized, and the
 419 proppant transport and fluid flow analysis were carried out at different time steps with fluid
 420 leak-off from the fracture wall, based on our proposed proppant transport model detailed in Suri
 421 et al.³⁸. This is an iterative process where the pressure field and fluid leak-off along the fractures
 422 was exchanged at each time step to model the proppant transport in dynamic fracture
 423 propagation, as shown in Fig. 6. The fluid and proppant mixture is injected at the inlet using
 424 velocity inlet boundary condition. To model the fluid leak-off from the fracture wall, a user-
 425 defined function is used to add a source term in the continuity and momentum transport
 426 equations. The amount of fluid leaking off from the fracture wall is obtained from the XFEM
 427 model that was used in the user-defined function. The detailed explanation of the CFD
 428 modelling parameters, boundary conditions and user-defined function can be found in our
 429 previous work.³⁸

430
 431

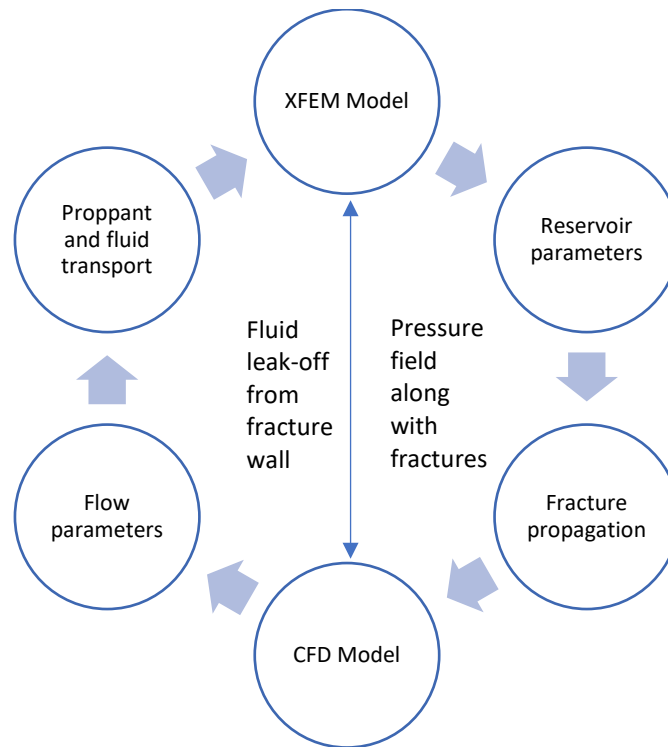
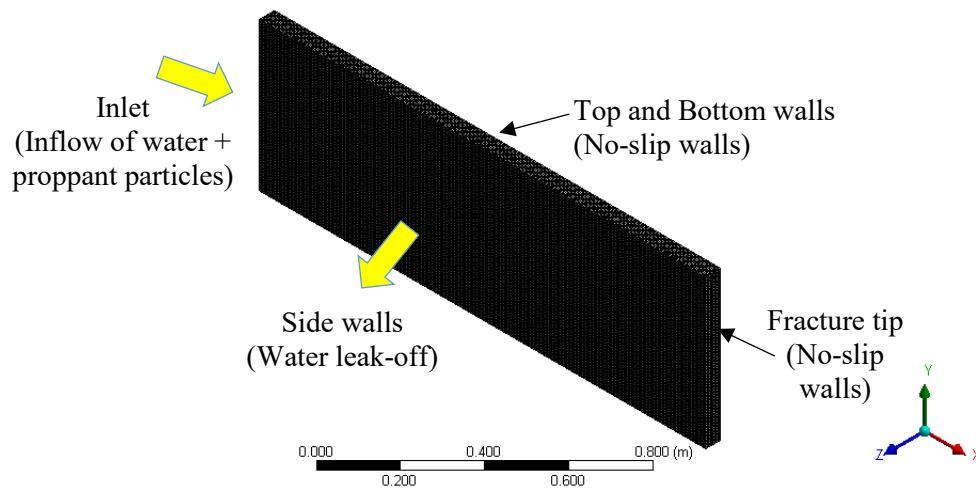


Fig. 6. XFEM-CFD coupling workflow

432
433

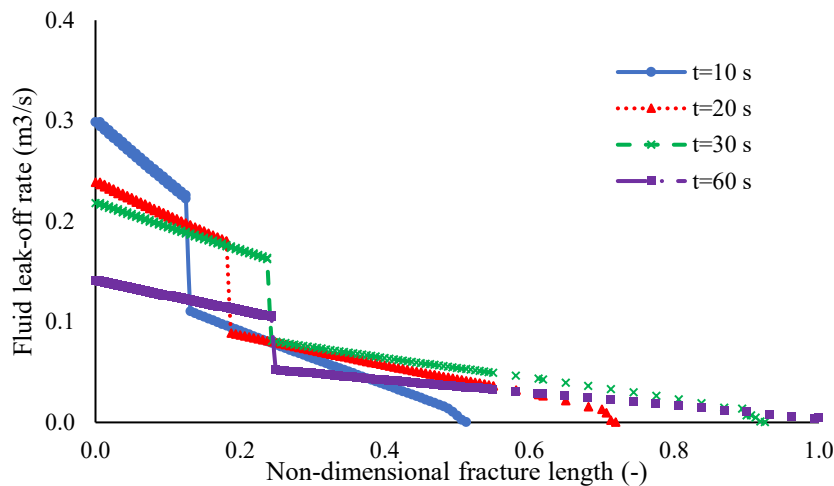
434 *2.6. Numerical modelling parameters*

435 Proppant transport and distribution were investigated in a hydraulic fracture using the CFD
 436 technique in ANSYS FLUENT. As the fracture propagates with time, the fracture geometry
 437 varies with time steps. The fracture geometry at different time step was imported into the CFD
 438 model from the XFEM model to study proppant transport. A typical fracture geometry or
 439 computational domain at a particular time step is shown in Fig. 7 that illustrates the boundary
 440 condition used in the current study. Firstly, the mesh of the fracture geometry is created so that
 441 it reasonably provides the mesh independent, numerically converged and computationally
 442 efficient solution. The fracturing fluid and proppants were injected together at the inlet with
 443 the volumetric inlet flow rate of 0.0025 m³/s. The density and viscosity of the fracturing fluid
 444 is assumed as 1000 kg/m³ and 1 cP (0.001 Pa-s). The density of proppants assumed is 2650
 445 kg/m³ with proppant size based on 20/40 sand and proppant volume fraction of 0.10. The no-
 446 slip wall condition was used at the top wall, bottom wall and fracture tip, as shown in Fig. 7.
 447 In order to mimic the fluid leak-off into the surrounding porous rock, the fluid leakage effect
 448 is modelled through the fracture sidewalls with the help of a user-defined function (UDF). The
 449 momentum and mass source terms are explicitly defined in the governing transport equations
 450 (Eqs. (28) and (30)) through UDF. The underlying equations describing the source terms and
 451 UDF used to model the fluid leak-off is explained in detail in our previous work.³⁸ The fluid
 452 leak-off profile along the fracture length to a surrounding porous medium obtained from the
 453 XFEM model at different time steps is shown in Fig. 8.
 454



455
456

Fig. 7. A typical fracture geometry to investigate proppant transport



457
458
459

Fig. 8. The fluid leak-off rate at different time steps

460 The pressure-based solver with transient state simulation was used to solve the proppant
461 transport equations. The effect of gravity was included in the simulation. In order to model the
462 turbulence in the flow, the Shear Stress Transport (SST) $k-\omega$ model⁶⁷ was used that blends the
463 standard $k-\omega$ turbulent model near the wall with the standard $k-\epsilon$ turbulent model in the free-
464 stream.⁶⁸ The simulation time step used was 0.001 s. The phase-coupled SIMPLE algorithm
465 and the node-based averaging scheme is used as a solution method for pressure-velocity
466 coupling^{68,69} and to apply the parcel approach, respectively.⁷⁰ Lastly, the second-order upwind
467 scheme was used to discretize and solve the governing equations.

469 3. Results and discussion

470 3.1. Validation

471
472
473
474
475
476

The proposed XFEM model in the current study is validated using the two different approaches.
Firstly, using the zero-toughness plane strain analytical model⁷¹ and secondly, using the real
field data. The validation using the analytical model is described below, and the validation using
the real field data is described in section 3.1.2.

477 3.1.1. Zero toughness plane strain fracture propagation model

478
479

The fracture propagation using the XFEM model was compared against the analytical results
from the zero-toughness plane strain model from Adachi⁷¹ using the geomechanical properties,

480 as shown in Table 1. The solution from plane strain model assumes impermeable elastic
 481 medium with negligible fracture toughness. Adachi⁷¹ proposed the dimensionless variables of
 482 length, fracture width, net fluid pressure and flow rate to derive the zero-toughness solution of
 483 2D hydraulic fracture propagation using the first-order approximation (Eq. (53)). Adachi⁷¹
 484 described that the proposed analytical model could successfully model the asymptotic
 485 behaviour of fracture opening and fluid pressure in the near tip region.

$$\bar{\Omega}_{m0}^{(1)} = A_0(1 - \xi^2)^{2/3} + A_1^{(1)}(1 - \xi^2)^{5/3} + B^{(1)} \left[4\sqrt{1 - \xi^2} + 2\xi^2 \ln \left| \frac{1 - \sqrt{1 - \xi^2}}{1 + \sqrt{1 - \xi^2}} \right| \right] \quad (53)$$

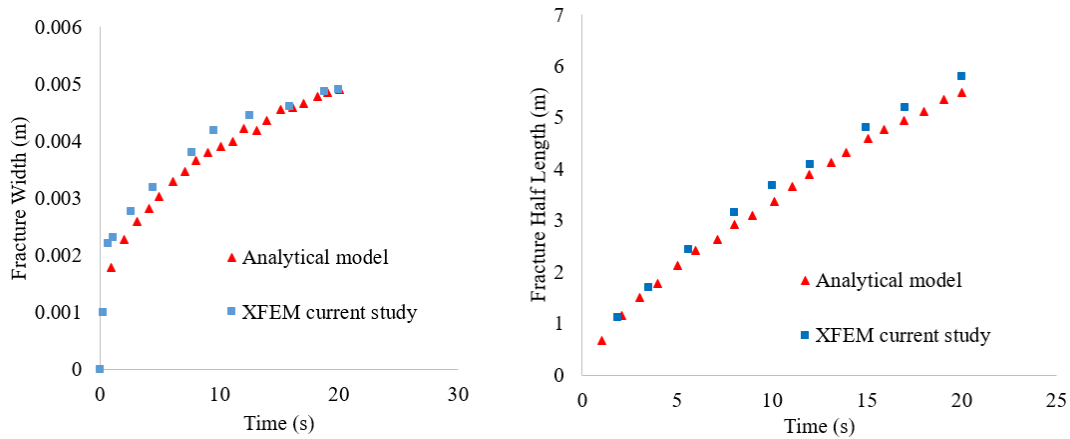
486 Where A_0 , $A_1^{(1)}$ and $B^{(1)}$ are constants, B is the Euler beta function, ξ is the length scaling
 487 factor. $\bar{\Omega}_{m0}^{(1)}$ is the dimensionless fracture width. The detailed derivation and explanation of the
 488 zero-toughness model can be found in Adachi⁷¹ and Adachi and Detournay⁷².
 489 The geomechanical and flow properties used in the comparison of current XFEM based
 490 simulation and an analytical model is detailed in Table 1.

491 Table 1

492 Geomechanical and flow properties for comparison with an analytical model

Parameter	Value
Elastic modulus	30 GPa
Poisson's ratio	0.3
Stress intensity factor	0.956 MPa.m ^{1/2}
Fluid viscosity	5.0 Pa.s
Fluid injection rate	0.001 m ³ /s

494 Fig. 9 shows the fracture propagation after 20 s of injection in terms of fracture width or fracture
 495 aperture and fracture half-length. The graph shows a reasonable match with a percentage error
 496 of 2% between the XFEM based numerical model and the zero-toughness analytical model.
 497 The results suggest that the XFEM model can be used for a detailed analysis of fracture
 498 propagation in porous media.
 499



500 Fig. 9. Comparison of the current model with an analytical model

501 3.1.2. Validation using the real field data

502 In order to study the dynamic fracture propagation with fluid flow and proppant transport, the
 503 real field data was used by Saberhosseini et al.³³. The field is located offshore in the Persian
 504 Gulf and consists of a tight limestone oil reservoir. The reservoir and geological properties used
 505 in the current study are detailed in Table 2. A detailed description of geology and reservoir
 506 characteristics can be found in Saberhosseini et al.³³.
 507
 508
 509
 510

511 Table 2
 512 Reservoir and geological properties

Property	Value
Porosity	0.10
Elastic Modulus	27.2 GPa
Permeability	2 mD
Poisson's ratio	0.22
Fluid viscosity	1 cP
Injection flow rate	0.0025 m ³ /s
Stress (vertical, maximum horizontal, minimum horizontal)	(47.61 MPa, 54.42 MPa, 40.81 MPa)
Pore pressure	23.43 MPa

513
 514 The semi-circular reservoir geometry with a diameter of 160 m is used in the current study, as
 515 shown in Fig. 10. The height of the reservoir is assumed as constant 20 m. The perforation or
 516 the initial location of the crack was defined using the XFEM method in Abaqus, as shown in
 517 Fig. 10. The fracturing operation is started with an injection rate of 0.0025 m³/s, and the fluid
 518 injection is maintained for 20 min. The in-situ geological properties and geomechanical stresses
 519 are presented in Table 2. The XFEM model is a conglomerate of cohesive zone material and
 520 porous rock. The cohesive zone material is located at the centre of the computational domain
 521 around the perforation. It is surrounded by porous rock. The fluid is injected at a high injection
 522 rate such that when the fracture propagation criteria are reached, the fracture starts propagating
 523 and the fluid leaks into the surrounding porous rock. With the progression of time, the fracture
 524 is propagated, and the fracture profile is extracted and imported into the CFD module to study
 525 the proppant transport and distribution. The height of the fracture is assumed as constant for
 526 simplicity. The computational domain is discretised, and enriched elements are assigned for
 527 arbitrary fracture propagation based on the in-situ stress. The enriched elements consist of
 528 displacement and pore pressure degrees of freedom that aids in fracture propagation. Uniform
 529 pore pressure and initial stresses are defined based on the real field data shown in Table 2. The
 530 fluid flow and proppant transport are explicitly modelled using CFD technique, and the
 531 proppant distribution with fracture propagation is analysed at different time steps.
 532 The rock geomechanical properties, such as Poisson's ratio, elastic modulus and rock tensile
 533 strength, play a critical role in the fracture initiation and propagation. Since these are material
 534 properties and are dependent on the characteristics of rock, thus it is a static parameter in the
 535 fracture propagation study. On the contrary, the controllable parameters in the hydraulic
 536 fracturing design are the fluid injection rates, fluid viscosity or fluid rheological properties,
 537 fluid leak-off, and type of proppants. Thus, an improved understanding of the effects of these
 538 parameters along with fluid-proppant interactions, proppant distribution in fracture initiation
 539 and fracture propagation can overcome the challenge of fracturing job failure in the petroleum
 540 industry.
 541 The computational domain was discretised to add the enriched elements, and the mesh is shown
 542 in Fig. 10. The mesh consists of 30,000 elements to accurately capture the fracture propagation.
 543 A very fine mesh is used surrounding the region where the perforation is located, as shown in
 544 the zoomed image of Fig. 10, because the large stress, pressure gradients and displacement are
 545 located there, and to capture the fracture mechanics accurately. As described earlier, the
 546 formation is modelled as a poroelastic material with the key rock mechanical and porous rock
 547 properties shown in Table 2. The traction-separation law is used, which is explained earlier in
 548 the methodology (section 2.3). The hydraulic fracturing fluid is assumed as incompressible with
 549 a viscosity of 1 cP. In order to model the in-situ stress and pore pressure, a geostatic step is used
 550 in Abaqus to achieve a stress equilibrium condition before a hydraulic fracture initiation.
 551 Following that, the fracturing fluid is injected at a sufficiently high rate so that the hydraulic
 552 pressure gradually increases and once the fracture propagation criteria are reached, the fracture
 553 starts propagating.

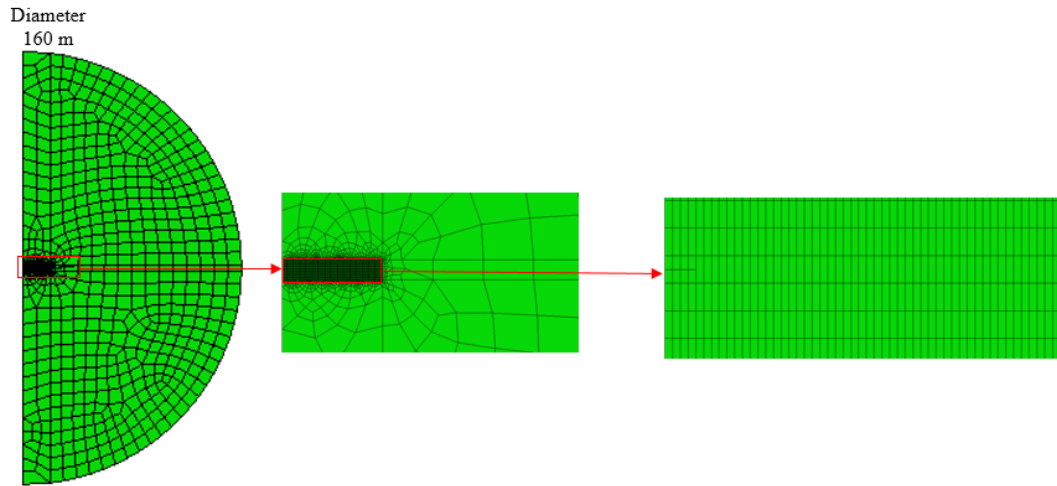


Fig. 10. Computational domain and mesh

554
555
556
557
558
559
560
561
562
563
564
565
566
567
568
569

Next, to ensure the applicability of the proposed numerical model, the results obtained were compared with the real field data with the reservoir and geological parameters, as described in Table 2. The fracture initiation pressure from both numerical simulation and the published real field case results³³ were compared. From Fig. 11, the equivalent fracture pressure from the numerical XFEM simulation using the same parameters as stated in Table 2 is evaluated as 7497 psi or 51.69 MPa. Moreover, the actual fracture pressure from the field after 20 min of injection time is 7500 psi or 51.02 MPa, as stated in Saberhosseini et al.³³. Comparing the fracture initiation pressure using XFEM method and actual measured value provides the percentage error of 0.04%, which shows a good agreement. Thus, the current XFEM model can simulate the fracture mechanics accurately as verified against the zero-toughness analytical model and with the real field result. This represents that the current XFEM model can accurately simulate the fracture propagation and can be employed for detail investigation of proppant transport and fluid flow in dynamic fracture propagation.

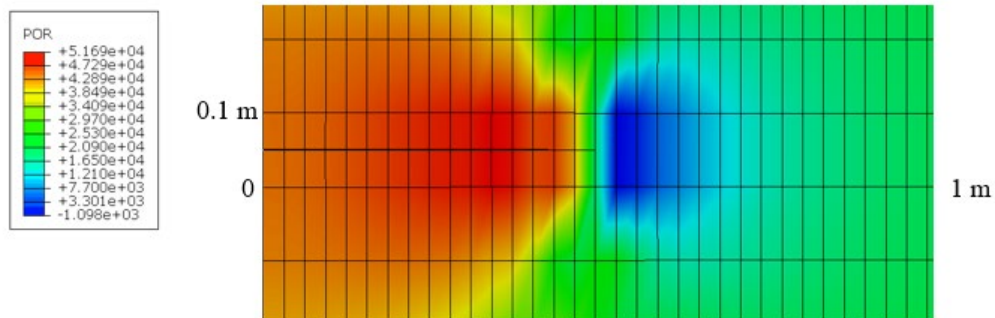
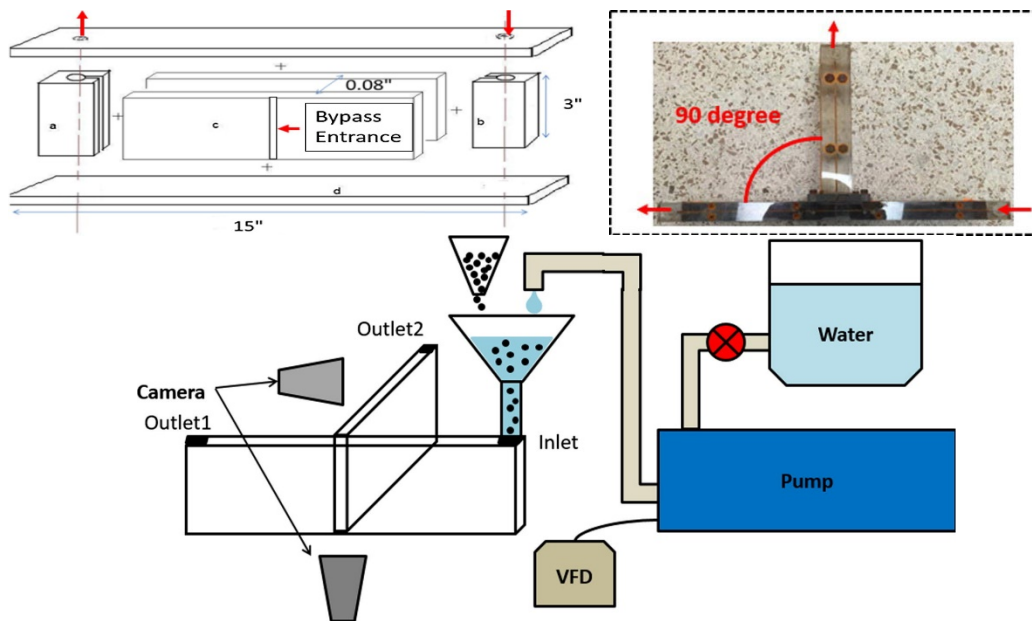


Fig. 11. Fracture initiation pressure from XFEM model

570
571
572
573
574
575
576
577
578
579
580
581
582
583
584

3.1.3. Comparison of CFD proppant transport model with the experimental results- Tong and Mohanty⁷³ performed an experimental study of proppant transport in fracture slots at different injection rates, which was used to compare the numerical results from the present hybrid CFD proppant transport model. The experiment consisted of two transparent fracture slots, as shown in Fig. 12 at different bypass angles. The main fracture slot is called as a primary fracture slot, and the bypass fracture slot is called as a secondary fracture slot. The dimensions of the primary fracture slot were 0.381 m × 0.002 m × 0.0762 m in L×W×H, and the secondary slot were 0.1905 m × 0.002 m × 0.0762 m in L×W×H. The slick water slurry with the suspended proppants is injected using a progressive cavity pump and sand funnel through the inlet located at the right end of the main fracture slot, as shown in Fig. 12. The fracturing fluid slurry (water + proppants) is injected at the inlet at different flow rates or injection velocities (0.1, 0.2 and 0.3 m/s) and proppant concentration (0.038, 0.019, and 0.013). 20/40 size sand is used as a

585 proppant with a density of 2650 kg/m^3 . Water is used as a fracturing fluid with viscosity 1 cP
 586 and density 1000 kg/m^3 . The proppant transport was monitored and recorded with cameras as
 587 shown in Fig. 12. The proppant bed deposition after 40 s of injection for different flow rates (or
 588 injection velocities) is compared for both the numerical and experimental results and are shown
 589 in Fig. 13. For quantitative comparison, the fraction of proppant deposited in the secondary
 590 fracture slot over the primary fracture slot was calculated and plotted at different injection
 591 velocities for both, experimental and simulation results, as shown in Fig. 14. The comparison
 592 of results in Fig. 13 and Fig. 14 suggests a reasonable match between the numerical simulation
 593 and experiment with a percentage error of 3.2% and 3% for proppant bed height and length,
 594 respectively.
 595 The results suggest an overall good match between the numerical model and experiment, and
 596 the model can be used for the detailed investigation of the effect of fracture propagation in the
 597 hydrodynamics of proppant transport.
 598
 599



600 Fig. 12. Schematic of the proppant transport fracture slot experiment⁷³
 601

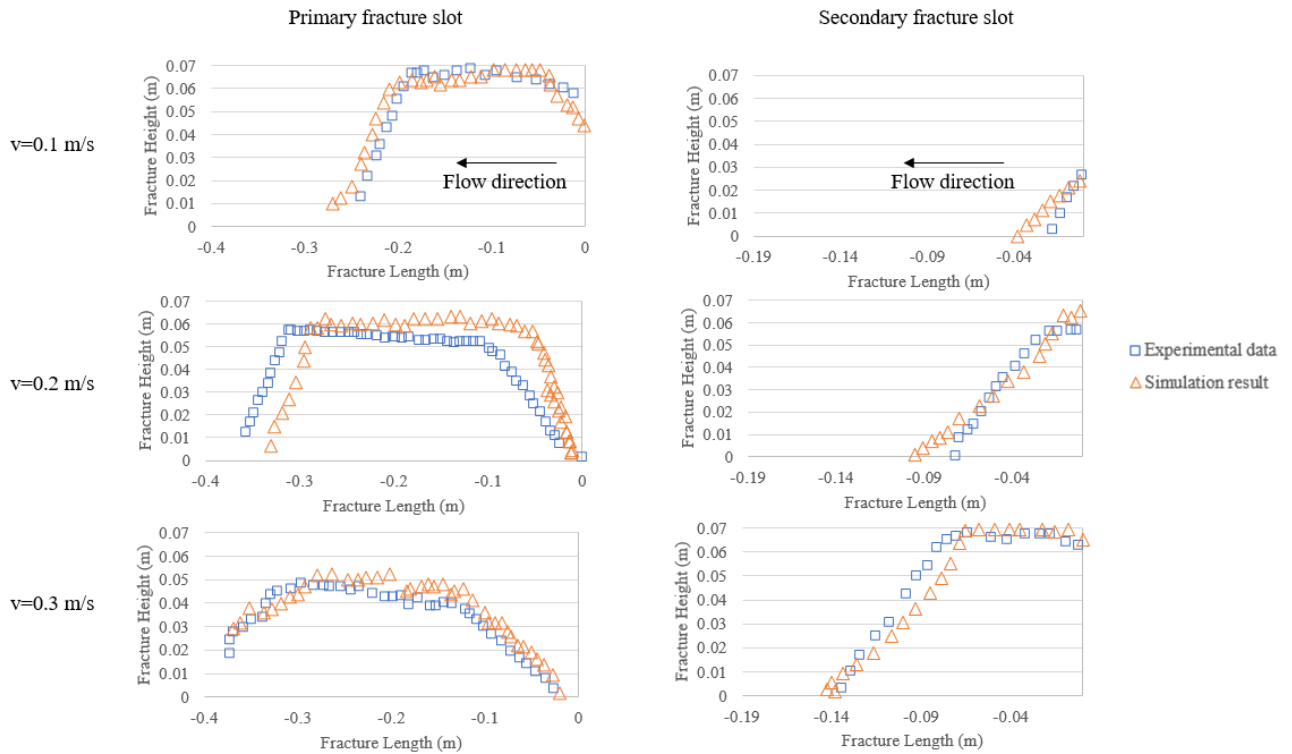


Fig. 13. Comparison of proppant bed deposition at $t=40$ s

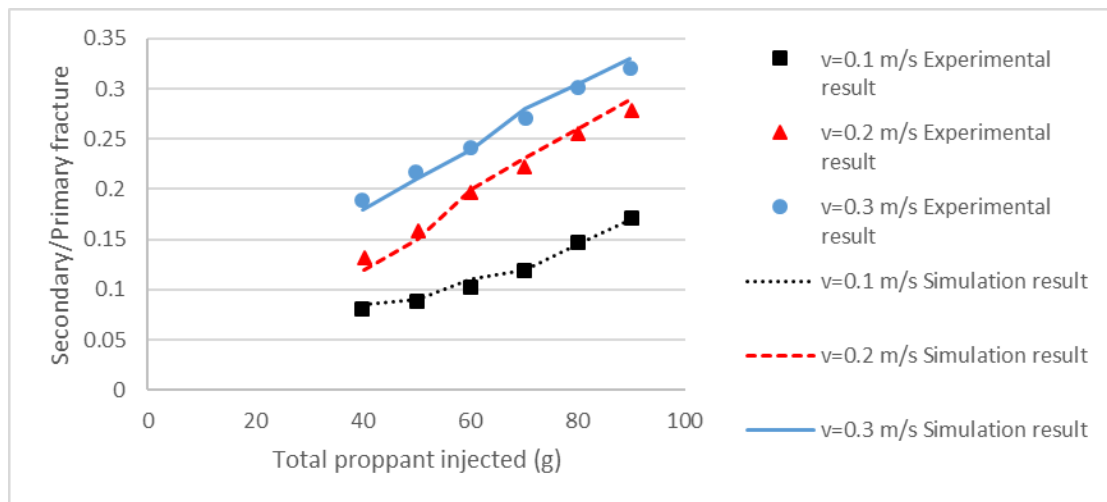


Fig. 14. Quantitative comparison of results – a fraction of proppant deposited in secondary/primary fracture slot at different injection velocities

3.2. Results of the base case

A base case fracture propagation simulation using XFEM was run with the parameters in Table 2. The base case simulates a hydraulic fracture propagation from perforation based on the defined in-situ stress, pore pressure and injection parameters. When the fracture initiation criteria are met, the fracture propagates in the direction of minimum fracture resistance. The proposed model provides the fracture propagation at every time step and accounts for the injection pressure, in-situ stresses, pore pressure distribution, and fracture trajectory. This information is vital as it has a direct impact on the design and success of hydraulic fracturing operation.

The fracture geometries at different time step are illustrated in Fig. 15, and the result of the fracture propagation using XFEM method with time is shown in Table 3. It can be seen from

619 Fig. 15 and Table 3 that once the fracture is initiated; the fracture propagates with time and as
 620 a result, the fracture length and fracture width increase. The fracture half-length increases
 621 abruptly towards the beginning as soon as the fracture is created. Subsequently, the fracture
 622 half-length gradually increases depending upon the injection flow rate and fluid leak-off.

623

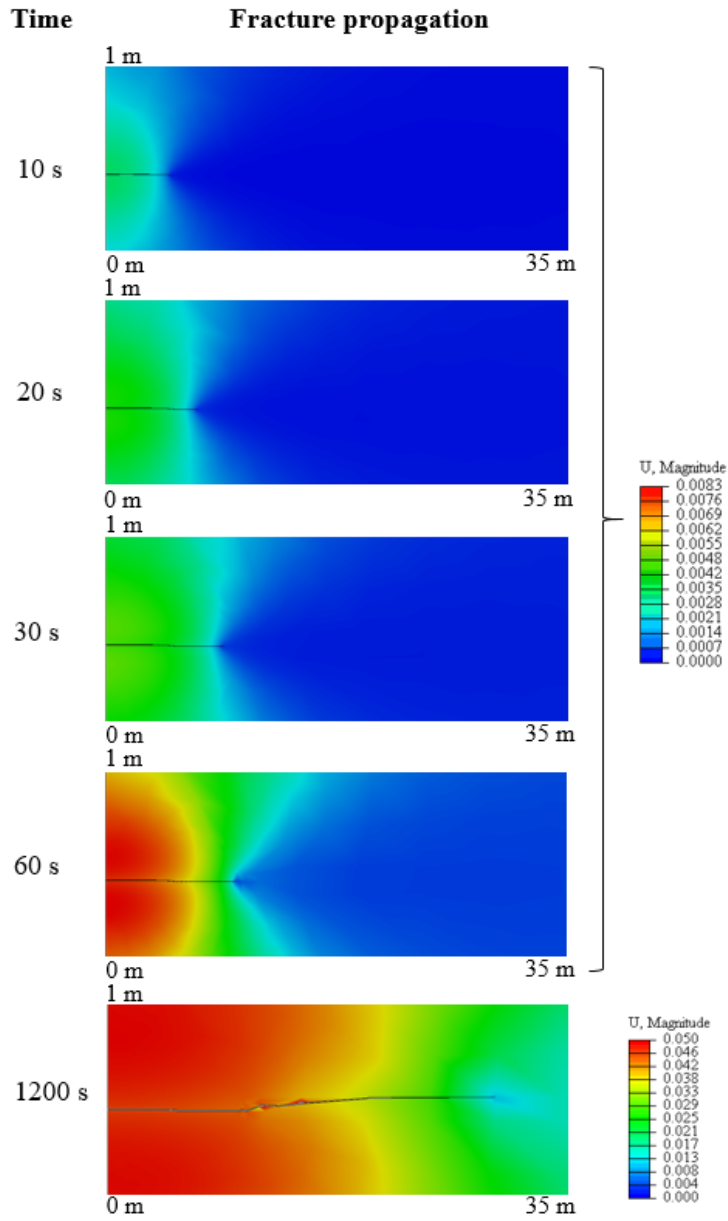
624 Table 3

625 Fracture propagation at different time steps

Time (s)	Fracture half-length (m)	Fracture width (m)
0	0.25	0
1	1	0.003
2.5	1.94	0.004
5	3	0.0049
7	4.06	0.0055
11	5.125	0.0063
16	6.125	0.0078
21	7.19	0.0085
26	8.25	0.009
30	9.19	0.0095
60	10.2	0.016
1021	30	0.082

626

627 Furthermore, to investigate the fluid flow and proppant transport with dynamic fracture
 628 propagation, the fracture profile from the XFEM at different time step and fluid properties were
 629 imported in Fluent and a detailed investigation using CFD proppant transport model was carried
 630 out. It is to be noted that the coupling between XFEM and CFD is achieved at each time step,
 631 only the fracture profile at specified time step is extracted from the XFEM to investigate the
 632 proppant transport within the fracture using CFD. The hybrid model for proppant transport is
 633 described earlier in section 2.4 and also in our previous work³⁸ is used for CFD modelling of
 634 proppant transport and distribution. The results from the proppant distribution at different time
 635 steps are shown in Fig. 16. The fracture half-length and fracture width in Fig. 16 at different
 636 time steps correspond to the fracture propagation length and fracture aperture from the XFEM
 637 fracture propagation model, and the height of the fracture is assumed as constant (0.5 m) for
 638 simplicity. It can be noticed in Fig. 16 that as the fluid-proppant mixture or slurry is injected
 639 into the fracture, part of fracturing fluid leak-off from the surrounding fracture wall into the
 640 porous media. The remaining fluid transport the proppant in the slurry into the fracture. Thus,
 641 due to the complex hydrodynamics of proppants, proppant-fluid and inter-proppant interaction,
 642 the proppant deposits away from the wellbore at the fracture bottom and forms a proppant bed.
 643 As the injection time increases, it results in fracture further propagating and increased proppant
 644 distribution into the fracture. Thus, the current study aims to capture this coupled phenomenon,
 645 and the key results obtained from the base case simulation in terms of proppant volume fraction
 646 contour plot is illustrated in Fig. 16.



647
648

Fig. 15. Fracture propagation at different time steps

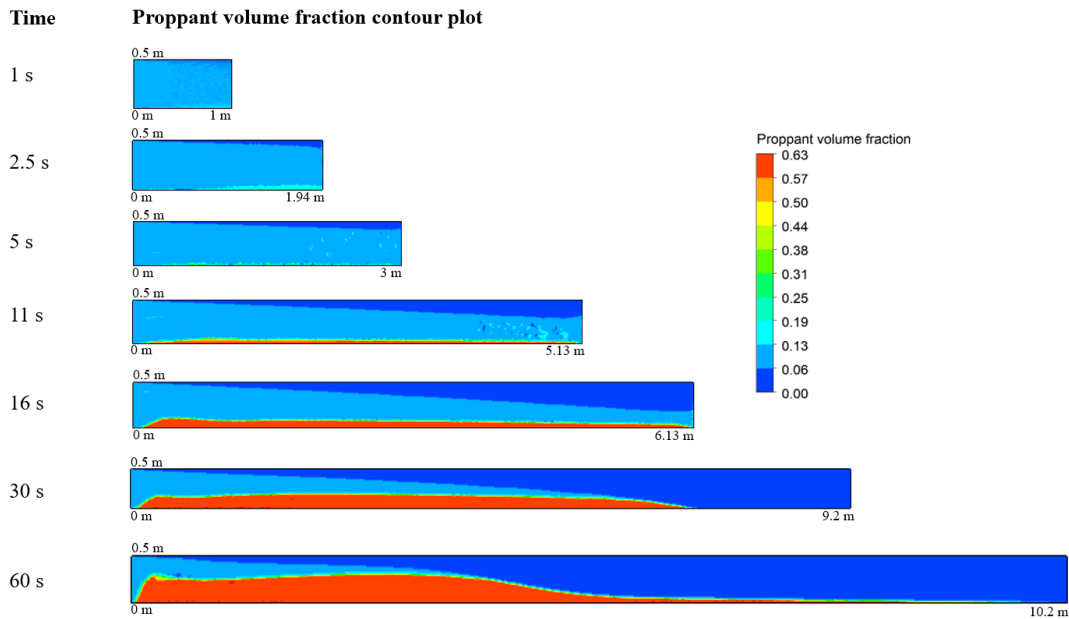


Fig. 16. Proppant transport in dynamic fracture propagation at different time steps

649
650

651 In order to investigate in detail, the impact of flow properties in efficient proppant distribution
652 and successful hydraulic fracturing design, different flow properties were varied. The role of
653 injection rate, fluid viscosity and leak-off rate constant is analysed in the propagation of fracture
654 and proppant distribution.

655

656 3.3. Fracture propagation as a function of injection rate

657

658 One of the most important controllable and yet essential parameters in the geometry of the
659 fracture and its optimisation is the injection rate during operation. It is well-known that by
660 increasing the injection rate, the dimensions of the fracture increase. Considering the
661 overburden and underburden defined as barriers that surround the reservoir, the operation
662 should be designed as if the mechanical and hydraulic integrity of these two barriers is
663 guaranteed. The accurate evaluation of width is another critical parameter to the optimal design
664 of the hydraulic fracturing because it directly dictates the size of proppant and also prevents the
665 risk of proppant bridging and screenout. Proppants are used so that the induced fracture remains
666 open and conducive. Moreover, by use of the validated numerical model, the real length of the
667 induced fracture can be accurately estimated. Knowing this length can help to increase it and
668 design to pass the disturbed area around the wellbore wall. This disturbed area created after
669 drilling and applying the drilling fluid can penetrate within the pores around the wellbore wall.
670 Increasing the length of the fracture to pass this area can enhance the production.

671

672 Thus, an investigation was carried out at three different injection rates $0.001 \text{ m}^3/\text{s}$, $0.0025 \text{ m}^3/\text{s}$
673 and $0.005 \text{ m}^3/\text{s}$ to understand the fracture propagation and proppant distribution. The results are
674 detailed in Table 4. Table 4 shows that with an increase in injection rate from $0.001 \text{ m}^3/\text{s}$ to
675 $0.005 \text{ m}^3/\text{s}$, the magnitude of fracture width and fracture half-length increases from 7.8 mm to
676 29 mm and 8 m to 12 m respectively. Therefore, the geometry of the induced fracture strongly
677 depends on the difference in the injection rate.

678

679

680

681

682 Table 4
 683 Fracture propagation with varying injection rate

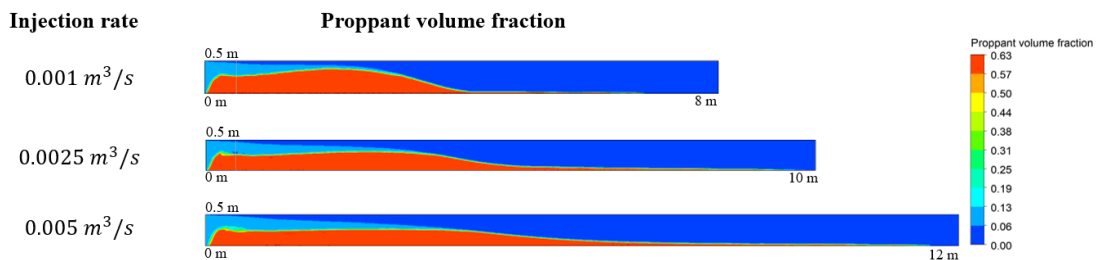
Injection rate (bbl/min)	Injection rate (m ³ /s)	Fracture width (m)	Fracture half-length (m)
0.4	0.0010	0.0078	8
1.0	0.0025	0.016	10
1.9	0.0050	0.029	12

684
 685 Fig. 17 details the comparison of proppant volume fraction at 60 s after injection for three
 686 different injection rates as described in Table 4. It can be interpreted from Fig. 17 that with the
 687 increase in injection rate, due to the higher slurry velocity, it adds more randomness in the flow
 688 which leads to greater proppant suspension ability in the fracturing fluid and consequently
 689 longer proppant transport. To quantitatively compare the results, the proppant volume fraction
 690 is calculated at two different cross-sectional planes located 2 m and 4 m from the inlet and
 691 plotted against the fracture height, as shown in Fig. 18. It can be noted from Fig. 18 that at x=2
 692 m from the inlet higher proppant bed is seen with 0.001 m³/s compared to 0.005 m³/s, due to
 693 more significant amount of proppant depositing near the wellbore having a lower velocity and
 694 ability to suspend in the slurry. On the contrary, at higher injection rate, i.e. 0.005 m³/s, the
 695 proppant is transported to a longer distance, as can be seen in Fig. 18 @x=4 m from the inlet.
 696 This is one of the significant challenges in the oil industry, especially when using slickwater
 697 for hydraulic fracturing in shales. The proppant tends to deposit quickly as soon as they are
 698 injected due to reduced ability of the slickwater to suspend proppants. Thus, the unpropped
 699 section of the fracture closes down resulting in loss of efficiency and production. An effort to
 700 transport the proppant to a longer distance can lead to an improved hydraulic fracturing design.

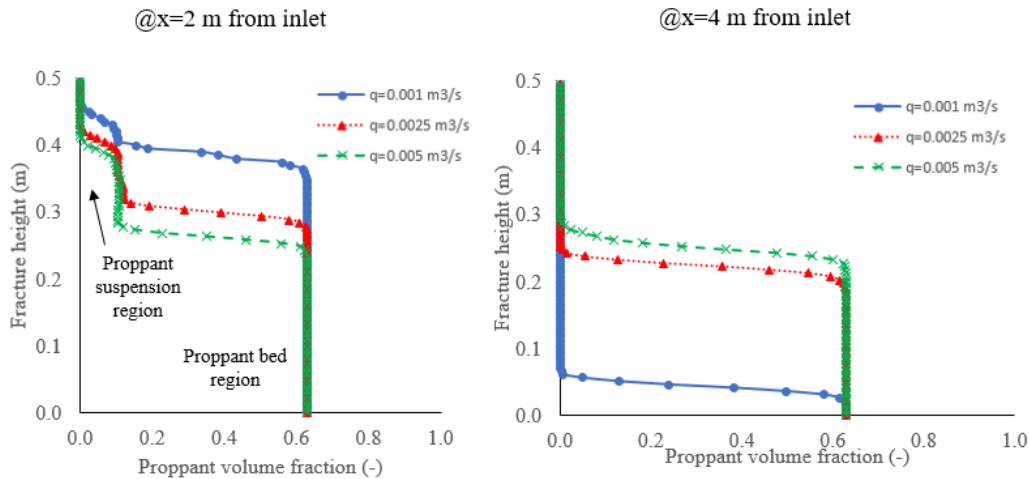
701
 702 Another frequently observed phenomenon seen during hydraulic fracturing that can lead to
 703 hydraulic fracturing design failure is that due to the proppant bridging, it can cause a fracture
 704 tip screen out. It means the proppant bed forms a bridge and does not allow the subsequent
 705 proppant injection to transport deeper into the fracture. This further result in an abrupt increase
 706 in pump pressure leading to hydraulic fracturing operation failure. This can be noticed in Fig.
 707 17 and Fig. 18 that with low injection rate, the proppant bridge has started to form and gradually
 708 it will result in fracture tip screen out. One of the parameters that can aid in preventing fracture
 709 tip screen out is by adequately controlling the injection rate.

710
 711 Similarly, the proppant horizontal transport velocity is plotted with fracture height at 60 s after
 712 injection at 2 m and 4 m from the wellbore. It can be noticed from Fig. 19 that near the wellbore
 713 the velocity profile of the cases q=0.0025 m³/s and q=0.005 m³/s are relatively similar. On the
 714 contrary, away from the wellbore, while the velocity of the case with q=0.001 m³/s is low, the
 715 case with q=0.005 m³/s still have higher velocity and thus ability to suspend proppant, resulting
 716 in more extended proppant transport. The results suggest that the increase in injection rate aids
 717 in more extended proppant transport by providing additional energy for the proppant suspension
 718 in the slurry.

719
 720

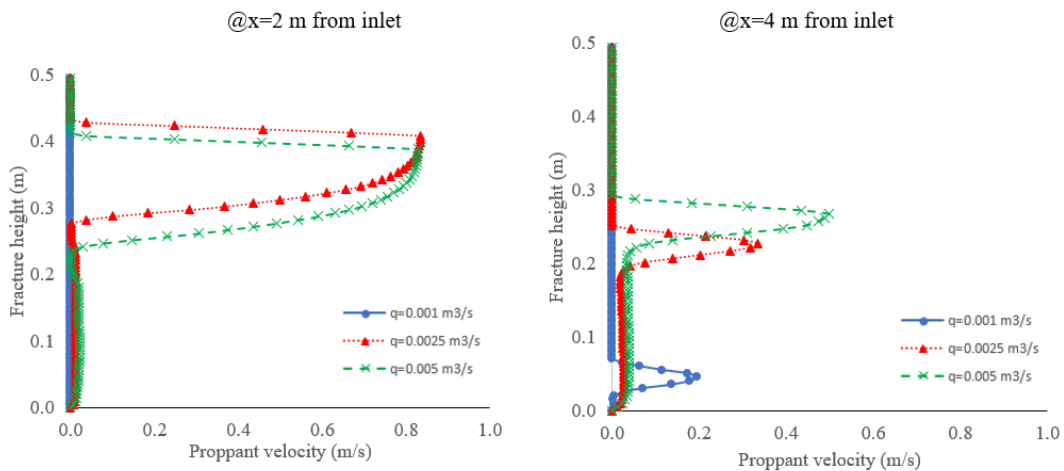


721
 722 Fig. 17. Proppant transport with dynamic fracture propagation at a varying injection rate



723
724
725
726

Fig. 18. Comparison of proppant distribution against fracture height at two different locations for varying injection rates

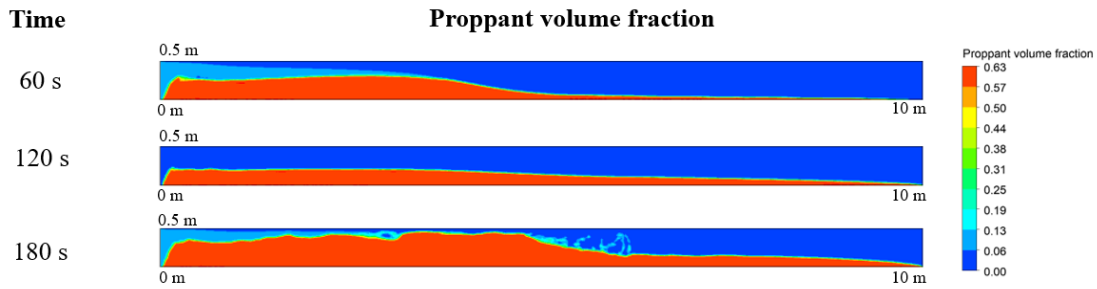


727
728
729
730

Fig. 19. Comparison of proppant horizontal velocity against fracture height at two different locations for varying injection rates

731 Another innovative approach that can aid in the success of hydraulic fracturing design by
732 preventing the fracture tip screenout and more extended proppant transport is injecting the
733 proppants intermittently and controlling the injection rate. It means that if a continuous stream
734 of proppant is injected with the fracturing fluid, depending upon the fracture height, the
735 proppant bridge will start developing after some time and will eventually result in fracture tip
736 screenout. However, if the proppant injection with fracturing fluid is followed by the pad fluid
737 with no proppant, the pad fluid will carry the proppant located towards the top of proppant bed
738 and transport it further inside the fracture. This phenomenon can be observed in Fig. 20, where
739 the proppant suspended in the slurry was injected till the 60 s, and then the pad fluid is injected
740 with no proppant for another 60 s. This intermittent injection is continued for two cycles, and
741 the results are compared in Fig. 20. To quantitatively understand the results of intermittent
742 injection, the proppant distribution is compared against the fracture height at different time
743 steps located at 2 m and 4 m from the wellbore and shown in Fig. 21. The results from Fig. 20
744 and Fig. 21 show that when the proppants are injected in the slurry for the first 60 s, the proppant
745 bridge started to build up in the form of proppant bed. Subsequently, when it is followed by the
746 injection of pad fluid for the next 60 s, the deposited proppants are transported further long into
747 the fracture with the pad fluid. This cycle is repeated with the injection of proppants with the
748 slurry for the next 60 s, and it can be noticed that for 180 s, nearly 60 % of the fracture is
749 successfully propped. Areal sweep efficiency of proppant distribution can be further improved

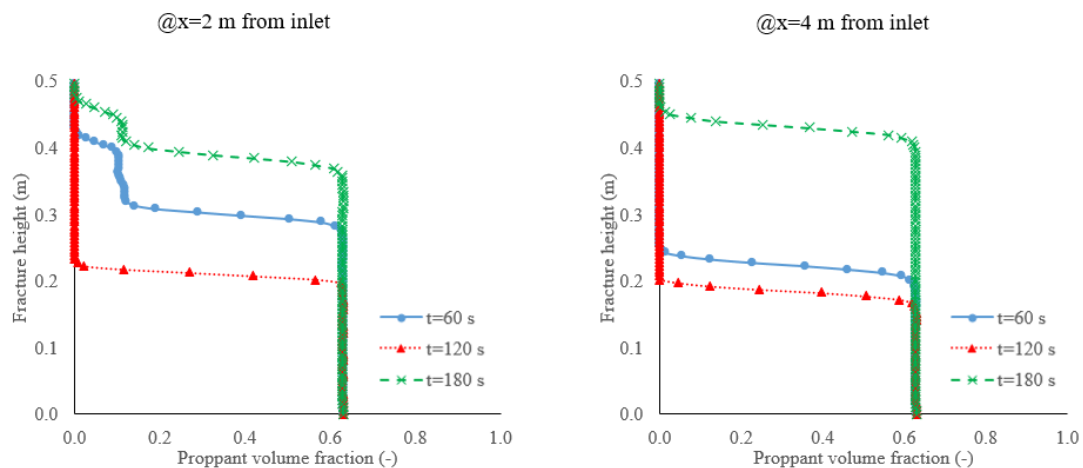
750 by subsequently following more intermittent injection cycles. This technique of intermittent
 751 injection can significantly improve the proppant distribution, enhance efficiency and fracture
 752 conductivity. The most significant advantage of using the intermittent injection and the
 753 proposed CFD-DEM Hybrid model is that it provides accurate proppant distribution and
 754 improved confidence to the petroleum engineers for a successful hydraulic fracturing design
 755 operation. This technique can help in overcoming the current challenge faced by the petroleum
 756 industry about low operational efficiency due to the unpropped fracture region. The unpropped
 757 region of the fracture closes down after the hydraulic pressure is removed.
 758



759
 760

Fig. 20. Proppant distribution at different time steps using intermittent injection.

761



762
 763

Fig. 21. Comparison of proppant distribution against fracture height at two different locations for intermittent injection at different time steps

764
 765

3.4. The impact of fracturing fluid viscosity on fracture propagation

766
 767

768 The fluid rheology plays a significant role in the proppant suspension during hydraulic
 769 fracturing operation³⁸. Thus, in this section, the impact of fracturing fluid viscosity in fracture
 770 propagation and proppant distribution is studied. The viscosity of fracturing fluid is increased
 771 from 0.1 to 1 and 10 cP, and the results of fracture propagation are shown in Table 5. It can be
 772 interpreted from Table 5 that as viscosity is increased from 0.1 to 10 cP, a significant increase
 773 in fracture opening from 14.5 mm to 18 mm and fracture half-length from 9 m to 11 m is
 774 observed. This can be explained by as the viscosity of the fracturing fluid is increased, it results
 775 in higher wellbore pressure acting on the fracture surface area and consequently greater force
 776 leading to an increase in fracture opening.
 777
 778

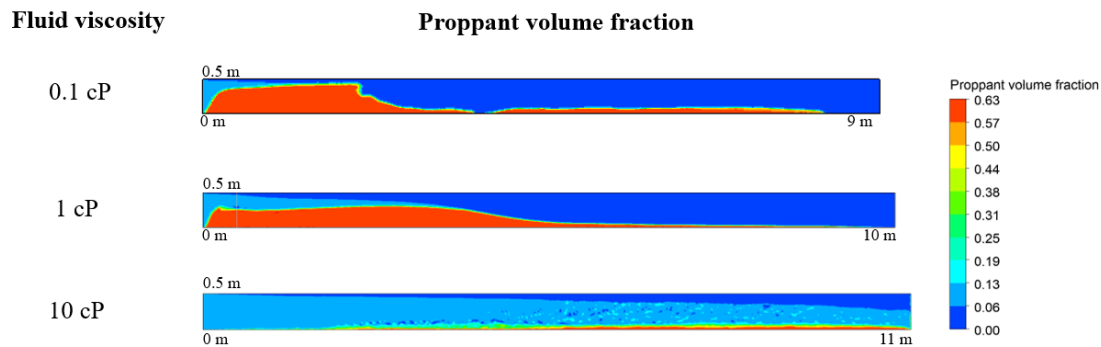
779
780

Table 5
Effect of fluid viscosity on fracture propagation

Fluid viscosity (cP)	Fluid viscosity (Pa.s)	Fracture width (m)	Fracture half-length (m)
0.1	0.0001	0.0145	9
1	0.001	0.016	10
10	0.01	0.018	11

781
782
783
784
785
786
787
788
789
790
791

Next, the effect of viscosity was also investigated in terms of proppant distribution and fluid flow. The results of proppant transport with different viscosities are shown in Fig. 22 in the form of a contour plot for proppant volume fraction. Fig. 22 shows that fluid viscosity can substantially influence the proppant transport. The lower viscosity fluid possesses the poor ability for proppant suspension, and consequently, the proppants are deposited quickly after injection resulting in the forming of proppant bridge. This further leads to a substantial area of fracture remaining unpropped and eventually closing down when the hydraulic pressure is removed. On the contrary, the higher viscosity fracturing fluid due to its better proppant suspension ability can suspend the proppants for a longer period and thus resulting in more extended proppant transport inside the fracture.



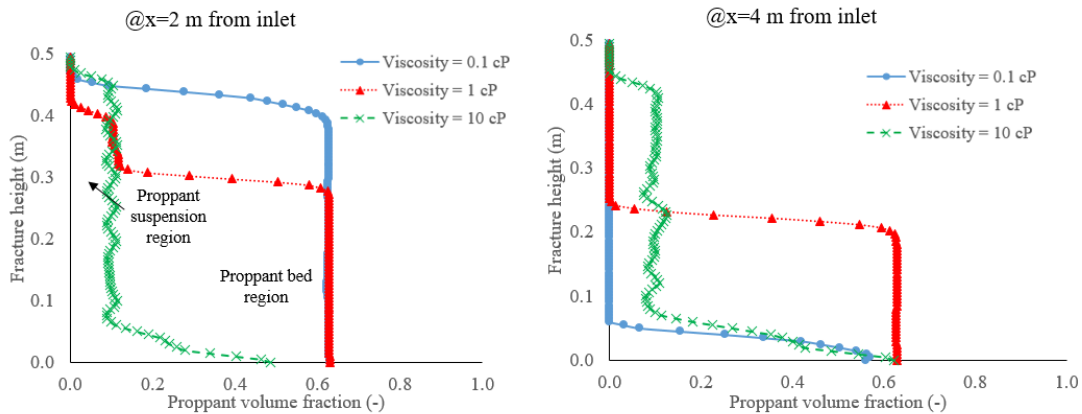
792
793

Fig. 22. Effect of viscosity on proppant transport

794
795
796
797
798
799
800
801
802
803
804
805
806
807
808
809
810
811
812
813
814
815
816
817

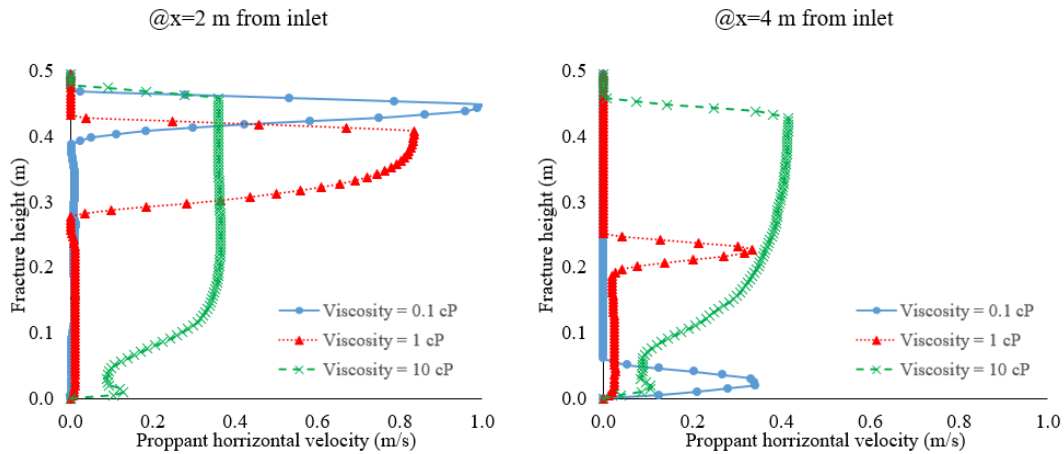
Similar to the analysis of variation in injection rate, proppant volume fraction and proppant horizontal velocity are computed and compared for different fluid viscosities at 2 m and 4 m from the wellbore, as shown in Fig. 23, and Fig. 24. Proppant distribution in Fig. 23 can be categorised into proppant bed and suspended proppants as shown. It can be seen that near the wellbore (@ 2 m from inlet), low viscosity fluid results in more significant proppant deposition as confirmed by the proppant bed almost reached the fracture height. This can further lead to a fracture tip screen out, as discussed earlier. On the contrary, for the high viscosity fluid, the proppant suspension region is substantially higher, and the proppant bed is minimal compared to other cases. However, away from the wellbore (@ 4 m from inlet), the low viscosity fluid has lower proppant bed and no proppant suspension region, as most of the proppant is deposited near the wellbore, and only a small number of proppants were able to reach this location. For the higher viscosity fluid, the proppants are still in suspension in good amount and tends to transport further deep into the fracture. This can be interpreted by the increasing viscous force contributes greater flow resistance and increases the amount of drag force on suspended proppants. This promotes the suspension ability of the proppants in the fluid and inhibits proppant deposition. Similar observations can also be noticed in Fig. 24, where proppant horizontal velocity was compared for all the cases. Near the wellbore at 2 m from the inlet, although the low viscosity fracturing fluid possesses higher velocity compared to high viscosity fluid, it has poor proppant suspension ability and thus away from the wellbore at 4 m from the inlet, the proppant in lower viscosity fluid lags behind the proppants in higher viscosity fluid. Thus, the investigation of fluid viscosity on dynamic fracture propagation and proppant transport suggested that as the fluid viscosity increases it leads to a relatively longer fracture propagation and improved suspension ability of the proppants, which aids in better proppant distribution in the fracture domain. Correctly modelling the proppant distribution using the

818 proposed model in an optimal fluid viscosity can help petroleum engineers to track the proppant
 819 distribution correctly and improve the hydraulic fracturing design.



820
 821
 822

Fig. 23. Effect of fluid viscosity on the proppant volume fraction



823
 824
 825
 826
 827

Fig. 24. Effect of fluid viscosity on proppant horizontal velocity

3.5. Influence of leak-off coefficient

828 In the oil and gas industry, it is widely recognised that the amount of fluid leak-off can
 829 significantly influence the hydraulic fracturing operation. However, to the best of our
 830 knowledge, no reported studies have investigated the impact of fluid leakage from the fracture-
 831 matrix interface to surrounding porous rock in proppant distribution and fracture complexity.
 832 To analyse the dynamic effects of fluid leakage in proppant distribution and fracture
 833 propagation, the fluid leak-off rate constant was varied from $5.0e-11$ m/kPa.s to $5.0e-9$ m/kPa.s.
 834 Fig. 25 shows the amount of fluid leakage for an increase in the non-dimensional fracture length
 835 with different leak-off constant and Fig. 26 shows the fluid leak-off profile as the fracture
 836 propagates with different time steps. The results show that as the leak-off rate increases, more
 837 fluid seeps into the surrounding porous reservoir. Moreover, the maximum amount of injected
 838 fluid is lost in the reservoir within the 15-30% of fracture length. This directly affects the
 839 proppant suspension ability and increases the rate of proppant deposition.

840
 841
 842
 843
 844
 845
 846

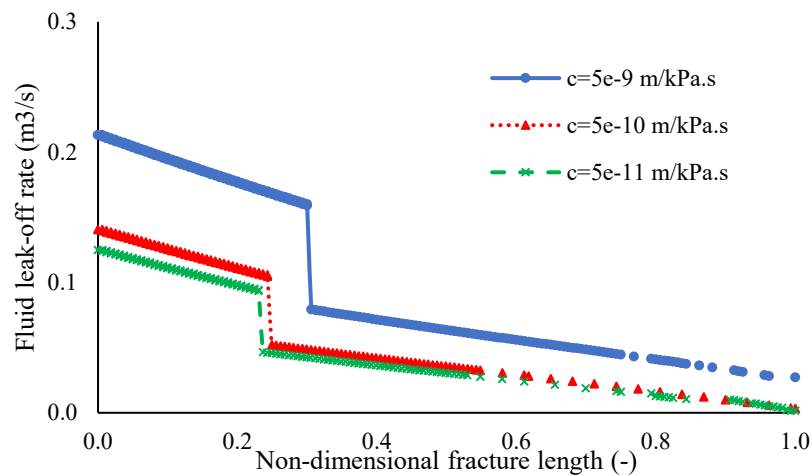
The fluid leaks-off from the fracture wall to the surrounding porous rock, leaving the proppants
 in the slurry and thus most of the proppants deposits at the fracture bottom leading to poor
 distribution of proppant away from the wellbore. Thus, modelling dynamic fluid leak-off in the
 proppant transport physics is crucial for the accurate prediction of proppant distribution and
 successful hydraulic fracturing design. The results from the net fracture width and fracture half-
 length observed by varying the leak-off rates are reported in Table 6. Table 6 shows that as the

847 amount of leak-off increases from 5.0×10^{-11} m/kPa.s to 5.0×10^{-9} m/kPa.s, it results in substantial
 848 lower fracture width from 18 mm to 10 mm and a relatively gradual reduction in fracture half-
 849 length from 11 m to 9.8 m. This can be explained by as the fluid leak-off increases from the
 850 fracture surface, and it results in significantly lower pressure acting on the fracture wall that
 851 facilitates fracture propagation acting against the minimum principal stress. This consequently
 852 leads to lower fracture width.

853
 854 Table 6
 855 Fracture propagation with different leak-off coefficient

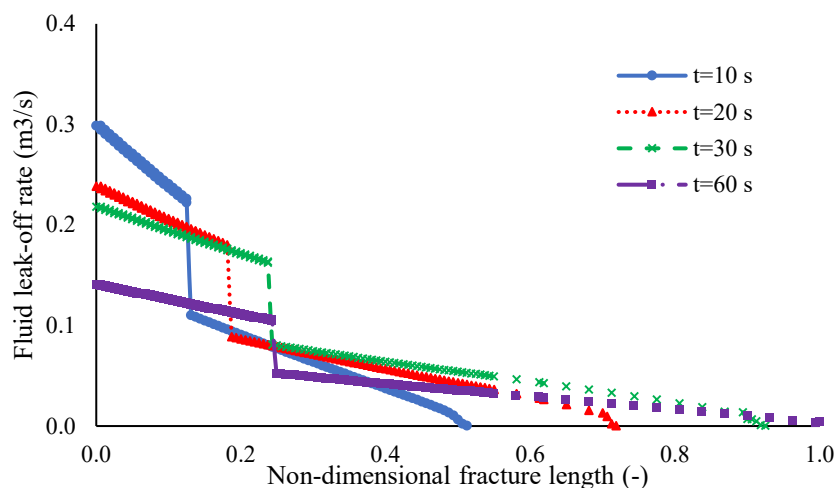
Leakoff constant (m/kPa.s)	Fracture width (m)	Fracture half length (m)
5×10^{-9}	0.01	9.8
5×10^{-10}	0.016	10
5×10^{-11}	0.018	11

856



857
 858

Fig. 25. Fluid leak-off profile along fracture length with the different leak-off coefficients



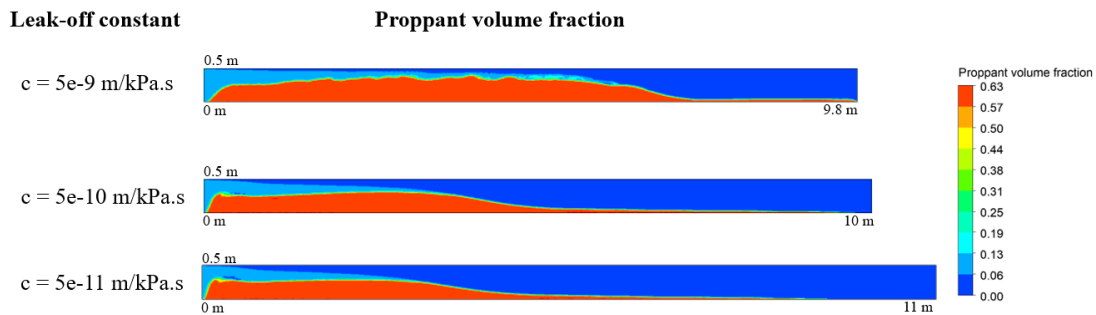
859
 860

Fig. 26. Fluid leak-off profile along fracture length at different time step

861 Next, the proppant distribution is investigated inside the fracture with varying leak-off rates.
 862 Fluid leakage from fracture-rock matrix interface characterises a pivotal role in the proppant
 863 suspension during hydraulic fracturing. As the fracturing fluid slurry enters into the fracture
 864 domain, the fracturing fluid leaks gradually through the fracture-rock matrix interface, and the
 865 remaining proppants in the slurry tend to deposit and form proppant bed at the fracture bottom.
 866 This can be evident in Fig. 27 that illustrates the proppant volume fraction for the different leak-

867 off rate constant. Fig. 27 shows that a higher proppant bed is noticed for the higher leak-off
 868 case. This can be explained by as the fracturing fluid seeps to the surrounding porous rock
 869 leaving behind the proppant in the remaining slurry, proppants tend to settle quickly forming
 870 greater proppant bed and consequently higher chances of early fracture tip screen-out. As
 871 explained earlier, the fracture tip screen out will then inhibit any further proppant transport into
 872 the fracture, and the unproped section of the fracture will close down, resulting in loss of
 873 fracture conductivity. On the contrary, the lower fluid leak-off rate case results in less amount
 874 of fluid leaking from the fracture to reservoir rock and thus can aid in proppant suspension with
 875 smaller proppant bed and more extended proppant transport into the fracture.
 876

877 The effect of fluid leakage from the fracture-matrix interface on the proppant distribution is
 878 usually ignored by the existing proppant transport models, and it can be noticed from Fig. 27
 879 that it can lead to inaccurate determination of proppants and inefficient hydraulic fracturing
 880 design. To quantitatively investigate the effects of fluid leak-off on fracture propagation and
 881 proppant distribution, a plot of proppant volume fraction and horizontal velocity with a fracture
 882 height are computed at 2 m and 4 m from the wellbore and are shown in Fig. 28 and Fig. 29. It
 883 can be seen that the higher fluid leak-off case with constant $5.0e-9$ m/kPa.s results in greater
 884 proppant bed deposition. This can be explained by a higher amount of fluid leaking-off from
 885 the fracture to reservoir matrix leaves the proppants inside the fracture. The settling velocity of
 886 the proppant becomes dominant to the horizontal transport velocity, and thus a more significant
 887 number of proppants tend to deposit. On the contrary, the lower leak-off rate case with constant
 888 $5.0e-11$ m/kPa.s, due to smaller amount of fluid leakage from the fracture-matrix interface,
 889 results in suspending and transporting proppant longer into the fracture, and thus lower number
 890 of proppants are deposited. Furthermore, comparing the proppant horizontal velocity in Fig. 29
 891 suggests that the higher velocity is noticed from higher leak-off rate case with constant $5.0e-9$
 892 m/kPa.s, compared to the other two cases. This can be explained by the higher leak-off results
 893 in lower fracture width during fracture propagation, as explained earlier. Thus, due to the lower
 894 fracture width, the volumetric injection flow rate is greater for the higher leak-off case.
 895 However, it can be noticed that even with the higher velocity in the case of higher leak-off
 896 constant, the proppants tend to deposit early as the settling velocity is dominant over the
 897 horizontal transport velocity because of greater fluid leakage from the fracture-matrix interface.
 898 The results from the variation of leak-off rate on proppant distribution suggest that fracturing
 899 fluid leak-off is one of the significant factors that govern the proppant distribution, fracture
 900 geometry and fracture conductivity. It is essential to include it in accurately modelling the
 901 proppant transport physics and hydraulic fracturing design.
 902
 903



904
 905 Fig. 27. Proppant distribution with varying leak-off rate constant

906
 907

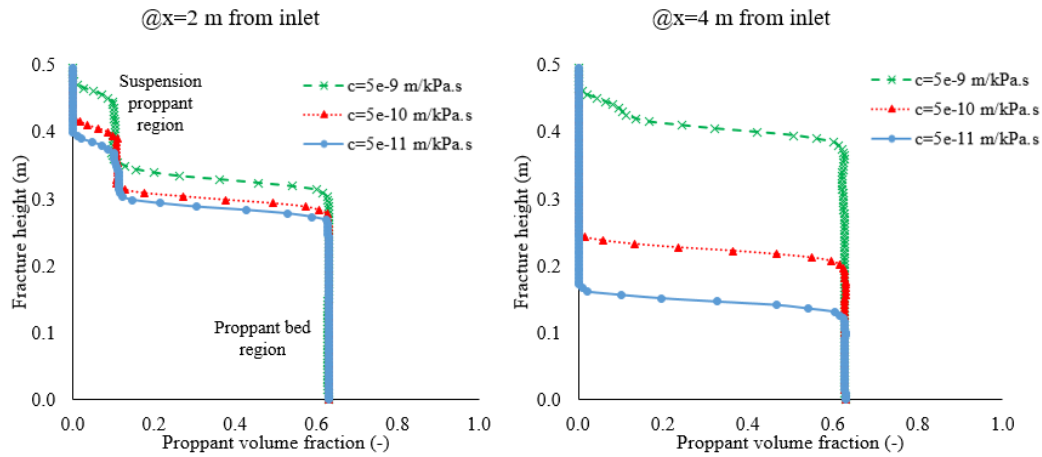


Fig. 28. Effect of the fluid leak-off rate constant on the proppant volume fraction

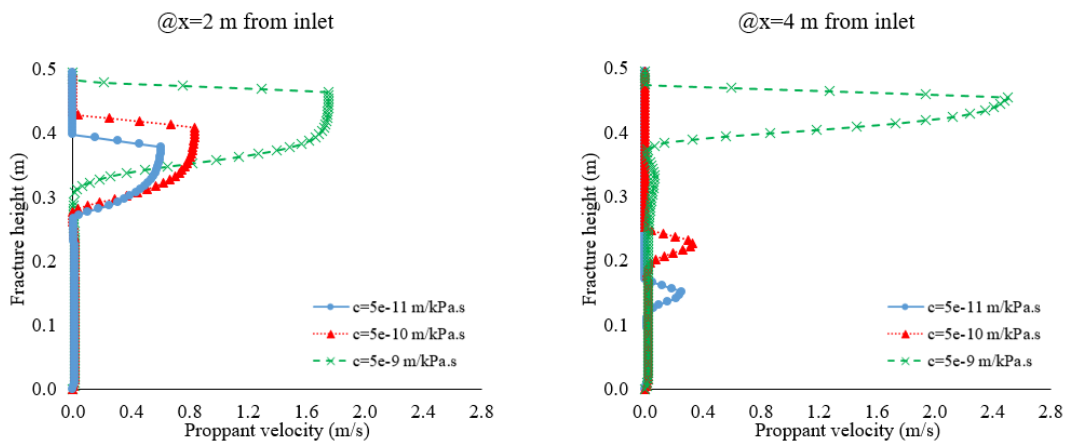


Fig. 29. Effect of the fluid leak-off rate constant on proppant horizontal velocity

4. Application in petroleum engineering

A successful hydraulic fracturing operation is designed such that the fracture is initiated and propagated with minimum tortuosity and complexities around the wellbore. In addition, the successful transport and settling of proppants inside the fracture domain also add to the success of hydraulic fracturing. The unproped section of fracture closes down due to the surrounding geomechanical stresses when the hydraulic pressure is removed. Thus, modelling accurately the fracture propagation coupled with proppant distribution is vital for the efficiency of hydraulic fracturing design. The propped fracture provides the desired conductivity and flow conduits for the reservoir fluids (oil or natural gas) to enter into the wellbore, and thus improve the production efficiency. Furthermore, another common failure in hydraulic fracturing design noticed in the oil industry is fracture tip screen-out. This happens when proppant in fracturing fluid, create a bridge inside the fracture and prevents any further transport of proppant and fluid, resulting in a rapid increase in pump pressure. Using advanced numerical models like the one proposed in the current study can aid in preventing the fracture tip screenout and model accurately proppant transport physics with dynamic fracture propagation.

Lastly, the numerical modelling results in this paper suggests that the reservoir characteristics and flow properties can significantly influence the fracture length, fracture width and proppant distribution inside the fracture. The coupled phenomenon of fluid flow, fracture propagation, proppant transport, fluid leakage, complex fluid-proppant and inter-proppant interactions can greatly influence the geomechanical stresses in the vicinity of the wellbore. This complex fracture mechanics and hydrodynamics of proppants cannot be modelled using analytical solutions or linear elastic models. Thus, the applicability of the proposed dynamic fracture

908
909
910

911
912
913
914
915
916
917
918
919
920
921
922
923
924
925
926
927
928
929
930
931
932
933
934
935
936

937 propagation and fluid flow model with proppant transport and fluid leakage can help petroleum
938 engineers to design the hydraulic fracturing operation with fewer limiting assumptions
939 successfully.

940 **5. Conclusions**

942 In this paper, a fully integrated model is proposed to dynamically model the fracture
943 propagation and proppant transport inside the fracture with fluid leak-off from the fracture
944 sidewall. The fracture propagation is modelled using the extended finite element method, and
945 the hydrodynamics of proppant transport is modelled using the computational fluid dynamics.
946 The numerical modelling results were compared against the zero toughness analytical model
947 and real field results, and a good agreement is obtained. The parametric study of injection rate,
948 fluid viscosity and fluid leakage is conducted that influence fracture propagation and proppant
949 distribution. The key conclusions obtained based on the parametric study are as follows-

- 950 1. Increase in injection rate aids in more extended proppant transport by providing
951 additional energy for the proppant suspension in the slurry.
- 952 2. Proppant bridging is a frequently observed phenomenon seen during hydraulic
953 fracturing depending upon the fracture height and width that can cause fracture tip
954 screen out and lead to hydraulic fracturing design failure. Intermittent proppant
955 injection technique is proposed and investigated to overcome this by controlling the
956 injection rate. It is observed that this technique of intermittent proppant injection can
957 significantly improve the proppant distribution, enhance areal sweep efficiency and
958 fracture conductivity.
- 959 3. The investigation of fluid viscosity on dynamics fracture propagation and proppant
960 transport suggested that as the fluid viscosity increases it leads to a relatively longer
961 fracture propagation and improved suspension ability of the proppants, which aids in
962 better proppant distribution in the fracture domain. Correctly modelling the proppant
963 distribution using the proposed model in an optimal fluid viscosity can help petroleum
964 engineers to track the proppant distribution correctly and improve the hydraulic
965 fracturing design.
- 966 4. The results from the variation of leak-off rate on proppant distribution suggest that
967 fracturing fluid leak-off is one of the significant factors that govern the proppant
968 distribution, fracture geometry and fracture conductivity. It is essential to include it in
969 accurately modelling the proppant transport physics and hydraulic fracturing design.
970 The higher leak-off rate can result in early proppant deposition and possibility of
971 fracture tip screen out.

972 The fully coupled XFEM-CFD model for dynamic fracture propagation and proppant transport
973 proposed in the current study overcomes the drawbacks of the existing proppant transport
974 models by accounting for cohesive based traction-separation law for fracture mechanics and
975 fluid leakage phenomenon through the fracture-rock matrix. These numerical modelling results
976 suggest that coupling the effects of the fracture propagation, proppant transport, fluid leakage,
977 complex fluid-proppant and inter-proppant interactions can significantly influence the
978 geomechanical stresses in the vicinity of the wellbore. Thus, the current model aids petroleum
979 engineers to successfully design the hydraulic fracturing operation and gain confidence in
980 tracking and distribution of proppants inside the fracture.

981 **Acknowledgement**

983 The authors are grateful to the School of Engineering, Robert Gordon University, Aberdeen,
984 United Kingdom, for supporting this research.

985 **Conflicts of Interest**

987 The authors declare no conflicts of interest.

992
993
994
995
996
997
998
999
1000
1001
1002
1003
1004
1005
1006
1007
1008
1009
1010
1011
1012
1013
1014
1015
1016
1017
1018
1019
1020
1021
1022
1023
1024
1025
1026
1027
1028
1029
1030
1031
1032
1033
1034
1035
1036
1037
1038
1039
1040
1041
1042
1043
1044
1045
1046

References

1. Chen Z, Bungler AP, Zhang X, Jeffrey RG. Cohesive zone finite element-based modeling of hydraulic fractures. *Acta Mechanica Solida Sinica*. 2009;22(5):443-452. [http://dx.doi.org/10.1016/S0894-9166\(09\)60295-0](http://dx.doi.org/10.1016/S0894-9166(09)60295-0).
2. Adachi J, Siebrits E, Peirce A, Desroches J. Computer simulation of hydraulic fractures. *Int J Rock Mech Min Sci*. 2007;44(5):739-757. <http://dx.doi.org/10.1016/j.ijrmms.2006.11.006>.
3. Zheltov YP, Khristianovic SA. Formation of vertical fractures by means of highly viscous liquid. In: Proceedings of the 4th world petroleum congress, 6-15 June, Rome, Italy. 1955.
4. Geertsma J, De Klerk F. A rapid method of predicting width and extent of hydraulically induced fractures. *J Pet Technol*. 1969;21(12):1,571-1,581. <https://doi.org/10.2118/2458-PA>.
5. Perkins T, Kern L. Widths of hydraulic fractures. *J Pet Technol*. 1961;13(09):937-949. <https://doi.org/10.2118/89-PA>.
6. Nordgren R. Propagation of a vertical hydraulic fracture. *Society of Petroleum Engineers Journal*. 1972;12(04):306-314. <https://doi.org/10.2118/3009-PA>.
7. Yew CH, Weng X. *Mechanics of hydraulic fracturing*. Gulf Professional Publishing; 2014.
8. Simonson E, Abou-Sayed A, Clifton R. Containment of massive hydraulic fractures. *Society of Petroleum Engineers Journal*. 1978;18(01):27-32. <https://doi.org/10.2118/6089-PA>.
9. Fung R, Vilayakumar S, Cormack DE. Calculation of vertical fracture containment in layered formations. *SPE Form Eval*. 1987;2(04):518-522. <https://doi.org/10.2118/14707-PA>.
10. Cleary MP, Kavvas M, Lam KY. Development of a fully three-dimensional simulator for analysis and design of hydraulic fracturing. In: Proceedings of the SPE/DOE Low Permeability Gas Reservoirs Symposium, 14-16 March, Denver, Colorado, USA. 1983. <https://doi.org/10.2118/11631-MS>.
11. Johnson Jr RL, Greenstreet CW. Managing uncertainty related to hydraulic fracturing modeling in complex stress environments with pressure-dependent leakoff. In: Proceedings of the SPE Annual Technical Conference and Exhibition, 5-8 October, Denver, Colorado, USA. 2003. <https://doi.org/10.2118/84492-MS>.
12. Advani SH, Lee T, Lee J. Three-dimensional modeling of hydraulic fractures in layered media: Part i—finite element formulations. *Journal of Energy Resources Technology*. 1990;112(1):1-9. <https://doi.org/10.1115/1.2905706>.
13. Siebrits E, Peirce AP. An efficient multi-layer planar 3D fracture growth algorithm using a fixed mesh approach. *Int J Numer Methods Eng*. 2002;53(3):691-717. <https://doi.org/10.1002/nme.308>.
14. Carter B, Desroches J, Ingraffea A, Wawrzynek P. Simulating fully 3D hydraulic fracturing. *Modeling in geomechanics*. 2000;200:525-557.
15. Barree R, Conway M. Experimental and numerical modeling of convective proppant transport. In: Proceedings of the SPE Annual Technical Conference and Exhibition, 25-28 September, New Orleans, Louisiana. 1994. <https://doi.org/10.2118/28564-MS>.
16. El-M. Shokir E, Al-Quraishi AA. Experimental and numerical investigation of proppant placement in hydraulic fractures. *Petrol Sci Technol*. 2009;27(15):1690-1703. <https://doi.org/10.1080/10916460802608768>.
17. Zhan J, Seetahal S, Cao J, et al. An integrated method to characterize shale gas reservoir performance. In: Proceedings of the SPE Trinidad and Tobago Section Energy Resources Conference, 13-15 June, Port of Spain, Trinidad and Tobago. 2016. <https://doi.org/10.2118/180884-MS>.
18. Ramurthy M, Barree RD, Broacha EF, Longwell JD, Kundert DP, Tamayo HC. Effects of high process-zone stress in shale stimulation treatments. In: Proceedings of the SPE Rocky Mountain Petroleum Technology Conference, 14-16 April, Denver, Colorado. 2009. <https://doi.org/10.2118/123581-MS>.
19. Behr A, Mtchedlishvili G, Friedel T, Haefner FK. Consideration of damaged zone in a tight gas reservoir model with a hydraulically fractured well. *SPE Production & Operations*. 2006;21(02):206-211. <https://doi.org/10.2118/82298-PA>.
20. Shaoul JR, Ross MJ, Spitzer WJ, Wheaton SR, Mayland PJ, Singh AP. Massive hydraulic fracturing unlocks deep tight gas reserves in india. In: Proceedings of the European

- 1047 Formation Damage Conference, 30 May-1 June, Scheveningen, The Netherlands. 2007.
1048 <https://doi.org/10.2118/107337-MS>.
- 1049 21. Frieauf KE. *Simulation and design of energized hydraulic fractures*. [Ph.D. Thesis]. The
1050 University of Texas at Austin; 2009.
- 1051 22. Zhang G, Liu H, Zhang J, Wu H, Wang X. Three-dimensional finite element simulation
1052 and parametric study for horizontal well hydraulic fracture. *Journal of Petroleum Science
1053 and Engineering*. 2010;72(3-4):310-317. <http://dx.doi.org/10.1016/j.petrol.2010.03.032>.
- 1054 23. Zhou L, Hou MZ. A new numerical 3D-model for simulation of hydraulic fracturing in
1055 consideration of hydro-mechanical coupling effects. *Int J Rock Mech Min Sci*. 2013;60:370-
1056 380. <http://dx.doi.org/10.1016/j.ijrmms.2013.01.006>.
- 1057 24. Fu P, Johnson SM, Carrigan CR. An explicitly coupled hydro-geomechanical model for
1058 simulating hydraulic fracturing in arbitrary discrete fracture networks. *Int J Numer Anal
1059 Methods Geomech*. 2013;37(14):2278-2300. <http://dx.doi.org/10.1002/nag.2135>.
- 1060 25. Ribeiro LHN. *Development of a three-dimensional compositional hydraulic fracturing
1061 simulator for energized fluids*. [Ph.D. Thesis]. The University of Texas at Austin; 2013.
- 1062 26. Wu Y, Li J, Ding D, Wang C, Di Y. A generalized framework model for the simulation of
1063 gas production in unconventional gas reservoirs. *SPE Journal*. 2014;19(05):845-857.
1064 <https://doi.org/10.2118/163609-PA>.
- 1065 27. Taleghani AD, Olson JE. Analysis of multistranded hydraulic fracture propagation: An
1066 improved model for the interaction between induced and natural fractures. In: Proceedings
1067 of the SPE Annual Technical Conference and Exhibition, 4-7 October, New Orleans,
1068 Louisiana. 2009. <https://doi.org/10.2118/124884-MS>.
- 1069 28. Keshavarzi R, Mohammadi S. A new approach for numerical modeling of hydraulic fracture
1070 propagation in naturally fractured reservoirs. In: Proceedings of the SPE/EAGE European
1071 Unconventional Resources Conference & Exhibition-From Potential to Production, 20-22
1072 March, Vienna, Austria. 2012. <https://doi.org/10.2118/152509-MS>.
- 1073 29. Zienkiewicz OC, Taylor RL, Zhu J. *The finite element method: Its basis and fundamentals*.
1074 Butterworth-Heinemann; 2013.
- 1075 30. Lecampion B. An extended finite element method for hydraulic fracture problems.
1076 *Communications in Numerical Methods in Engineering*. 2009;25(2):121-133.
1077 <https://doi.org/10.1002/cnm.1111>.
- 1078 31. Mohammadnejad T, Khoei A. An extended finite element method for hydraulic fracture
1079 propagation in deformable porous media with the cohesive crack model. *Finite Elements
1080 Anal Des*. 2013;73:77-95. <https://doi.org/10.1016/j.finela.2013.05.005>.
- 1081 32. Khoei A, Vahab M, Hirmand M. Modeling the interaction between fluid-driven fracture
1082 and natural fault using an enriched-FEM technique. *Int J Fract*. 2016;197(1):1-24.
1083 <https://doi.org/10.1007/s10704-015-0051-0>.
- 1084 33. Saberhosseini SE, Ahangari K, Mohammadrezaei H. Optimization of the horizontal-well
1085 multiple hydraulic fracturing operation in a low-permeability carbonate reservoir using fully
1086 coupled XFEM model. *Int J Rock Mech Min Sci*. 2019;114:33-45.
1087 <https://doi.org/10.1016/j.ijrmms.2018.09.007>.
- 1088 34. Moës N, Dolbow J, Belytschko T. A finite element method for crack growth without
1089 remeshing. *Int J Numer Methods Eng*. 1999;46(1):131-150.
1090 [https://doi.org/10.1002/\(SICI\)1097-0207\(19990910\)46:13.0.CO;2-J](https://doi.org/10.1002/(SICI)1097-0207(19990910)46:13.0.CO;2-J).
- 1091 35. Stolarska M, Chopp DL, Moës N, Belytschko T. Modelling crack growth by level sets in
1092 the extended finite element method. *Int J Numer Methods Eng*. 2001;51(8):943-960.
1093 <https://doi.org/10.1002/nme.201>.
- 1094 36. Sukumar N, Prévost J. Modeling quasi-static crack growth with the extended finite element
1095 method part I: Computer implementation. *Int J Solids Structures*. 2003;40(26):7513-7537.
1096 <https://doi.org/10.1016/j.ijsolstr.2003.08.002>.
- 1097 37. Marina S, Derek I, Mohamed P, Yong S, Imo-Imo EK. Simulation of the hydraulic
1098 fracturing process of fractured rocks by the discrete element method. *Environmental Earth
1099 Sciences*. 2015;73(12):8451-8469. <https://doi.org/10.1007/s12665-014-4005-z>.

- 1100 38. Suri Y, Islam SZ, Hossain M. A new CFD approach for proppant transport in
1101 unconventional hydraulic fractures. *Journal of Natural Gas Science and Engineering*.
1102 2019;102951. <https://doi.org/10.1016/j.jngse.2019.102951>.
- 1103 39. Chen Z. An ABAQUS implementation of the XFEM for hydraulic fracture problems. In:
1104 Proceedings of the ISRM International Conference for Effective and Sustainable Hydraulic
1105 Fracturing, 20-22 May, Brisbane, Australia. 2013.
- 1106 40. Shi F, Wang X, Liu C, Liu H, Wu H. An XFEM-based method with reduction technique
1107 for modeling hydraulic fracture propagation in formations containing frictional natural
1108 fractures. *Eng Fract Mech*. 2017;173:64-90.
1109 <https://doi.org/10.1016/j.engfracmech.2017.01.025>.
- 1110 41. Belytschko T, Black T. Elastic crack growth in finite elements with minimal remeshing. *Int*
1111 *J Numer Methods Eng*. 1999;45(5):601-620. [https://doi.org/10.1002/\(SICI\)1097-](https://doi.org/10.1002/(SICI)1097-0207(19990620)45:5%3C601::AID-NME598%3E3.0.CO;2-S)
1112 [0207\(19990620\)45:5%3C601::AID-NME598%3E3.0.CO;2-S](https://doi.org/10.1002/(SICI)1097-0207(19990620)45:5%3C601::AID-NME598%3E3.0.CO;2-S).
- 1113 42. Melenk JM, Babuška I. The partition of unity finite element method: Basic theory and
1114 applications. *Comput Methods Appl Mech Eng*. 1996;139(1-4):289-314.
1115 <https://doi.org/10.3929/ethz-a-004284735>.
- 1116 43. Fries T, Baydoun M. Crack propagation with the extended finite element method and a
1117 hybrid explicit-implicit crack description. *Int J Numer Methods Eng*. 2012;89(12):1527-
1118 1558. <https://doi.org/10.1002/nme.3299>.
- 1119 44. Wang H. Numerical modeling of non-planar hydraulic fracture propagation in brittle and
1120 ductile rocks using XFEM with cohesive zone method. *Journal of Petroleum Science and*
1121 *Engineering*. 2015;135:127-140. <https://doi.org/10.1016/j.petrol.2015.08.010>.
- 1122 45. Osher S, Sethian JA. Fronts propagating with curvature-dependent speed: Algorithms based
1123 on hamilton-jacobi formulations. *Journal of computational physics*. 1988;79(1):12-49.
1124 [https://doi.org/10.1016/0021-9991\(88\)90002-2](https://doi.org/10.1016/0021-9991(88)90002-2).
- 1125 46. Chang K. *Product performance evaluation using CAD/CAE: The computer aided*
1126 *engineering design series*. Academic press; 2013.
- 1127 47. Rabczuk T, Zi G, Gerstenberger A, Wall WA. A new crack tip element for the phantom-
1128 node method with arbitrary cohesive cracks. *Int J Numer Methods Eng*. 2008;75(5):577-
1129 599. <https://doi.org/10.1002/nme.2273>.
- 1130 48. Duan Q, Song J, Menouillard T, Belytschko T. Element-local level set method for three-
1131 dimensional dynamic crack growth. *Int J Numer Methods Eng*. 2009;80(12):1520-1543.
1132 <https://doi.org/10.1002/nme.2665>.
- 1133 49. Barenblatt GI. The mathematical theory of equilibrium cracks in brittle fracture. In:
1134 *Advances in applied mechanics*. Vol 7. Elsevier; 1962:55-129.
- 1135 50. Tomar V, Zhai J, Zhou M. Bounds for element size in a variable stiffness cohesive finite
1136 element model. *Int J Numer Methods Eng*. 2004;61(11):1894-1920.
1137 <https://doi.org/10.1002/nme.1138>.
- 1138 51. Chen J. Simulation of multi-directional crack growth in braided composite t-piece
1139 specimens using cohesive models. *Fatigue & Fracture of Engineering Materials &*
1140 *Structures*. 2011;34(2):123-130. <https://doi.org/10.1111/j.1460-2695.2010.01499.x>.
- 1141 52. Högberg JL. Mixed mode cohesive law. *Int J Fract*. 2006;141(3-4):549-559.
1142 <https://doi.org/10.1007/s10704-006-9014-9>.
- 1143 53. Haddad M, Sepehrnoori K. XFEM-based CZM for the simulation of 3D multiple-cluster
1144 hydraulic fracturing in quasi-brittle shale formations. *Rock Mech Rock Eng*.
1145 2016;49(12):4731-4748. <https://doi.org/10.1007/s00603-016-1057-2>.
- 1146 54. Riccio A, Saputo S, Raimondo A, Sellitto A. Modeling low velocity impact phenomena on
1147 composite structures. In: *Dynamic response and failure of composite materials and*
1148 *structures*. Elsevier; 2017:129-158. <https://doi.org/10.1016/B978-0-08-100887-4.00004-4>.
- 1149 55. Shojaei A, Shao J. *Porous rock fracture mechanics: With application to hydraulic*
1150 *fracturing, drilling and structural engineering*. Woodhead Publishing; 2017.
- 1151 56. Benzeggagh ML, Kenane M. Measurement of mixed-mode delamination fracture toughness
1152 of unidirectional glass/epoxy composites with mixed-mode bending apparatus. *Composites*
1153 *Sci Technol*. 1996;56(4):439-449. [https://doi.org/10.1016/0266-3538\(96\)00005-X](https://doi.org/10.1016/0266-3538(96)00005-X).

- 1154 57. Cristian MS, Paullo M, Roehl D. Continuation methods for the simulation of rock fracture
1155 with cohesive elements. In: Proceedings of the 13th ISRM International Congress of Rock
1156 Mechanics, 10-13 May, Montreal, Canada. 2015.
- 1157 58. Yao Y, Liu L, Keer LM. Pore pressure cohesive zone modeling of hydraulic fracture in
1158 quasi-brittle rocks. *Mech Mater.* 2015;83:17-29.
1159 <https://doi.org/10.1016/j.mechmat.2014.12.010>.
- 1160 59. Paul B, Faivre M, Massin P, et al. 3D coupled HM–XFEM modeling with cohesive zone
1161 model and applications to non planar hydraulic fracture propagation and multiple hydraulic
1162 fractures interference. *Comput Methods Appl Mech Eng.* 2018;342:321-353.
1163 <https://doi.org/10.1016/j.cma.2018.08.009>.
- 1164 60. Gidaspow D. *Multiphase flow and fluidization: Continuum and kinetic theory descriptions*.
1165 Academic press; 1994.
- 1166 61. Savage S, Jeffrey D. The stress tensor in a granular flow at high shear rates. *J Fluid Mech.*
1167 1981;110:255-272. <https://doi.org/10.1017/S0022112081000736>.
- 1168 62. Wachem BGMV, Schouten JC, Bleek CMVD, Krishna R, Sinclair JL. Comparative analysis
1169 of CFD models of dense gas–solid systems. *AIChE J.* 2001;47(5):1035-1051.
1170 <https://doi.org/10.1002/aic.690470510>.
- 1171 63. Lun C, Savage SB, Jeffrey D, Chepurmy N. Kinetic theories for granular flow: Inelastic
1172 particles in couette flow and slightly inelastic particles in a general flowfield. *J Fluid Mech.*
1173 1984;140:223-256. <https://doi.org/10.1017/S0022112084000586>.
- 1174 64. Basu D, Das K, Smart K, Ofoegbu G. Comparison of eulerian-granular and discrete element
1175 models for simulation of proppant flows in fractured reservoirs. In: Proceedings of the Paper
1176 IMECE2015-50050, ASME 2015 International Mechanical Engineering Congress and
1177 Exposition. Volume 7B: Fluids Engineering Systems and Technologies Houston, Texas,
1178 USA, 13-19 November, 2015. 2015:V07BT09A012. <https://doi.org/10.1115/IMECE2015-50050>.
- 1179 65. Gidaspow D, Bezburuah R, Ding J. Hydrodynamics of circulating fluidized beds: Kinetic
1180 theory approach. *Illinois Inst. of Tech., Chicago, IL (United States). Dept. of Chemical*
1181 *Engineering.* 1991.
- 1182 66. Johnson PC, Jackson R. Frictional–collisional constitutive relations for granular materials,
1183 with application to plane shearing. *J Fluid Mech.* 1987;176:67-93.
1184 <https://doi.org/10.1017/S0022112087000570>.
- 1185 67. Menter F. Zonal two equation kw turbulence models for aerodynamic flows. In:
1186 Proceedings of the 23rd fluid dynamics, plasmadynamics, and lasers conference. 1993:2906.
1187 <https://doi.org/10.2514/6.1993-2906>.
- 1188 68. Versteeg HK, Malalasekera W. *An introduction to computational fluid dynamics: The finite*
1189 *volume method*. Pearson Education; 2007.
- 1190 69. Patankar S. *Numerical heat transfer and fluid flow*. CRC press; 1980.
- 1191 70. Mahdavi M, Sharifpur M, Meyer JP. CFD modelling of heat transfer and pressure drops for
1192 nanofluids through vertical tubes in laminar flow by lagrangian and eulerian approaches. *Int*
1193 *J Heat Mass Transfer.* 2015;88:803-813.
1194 <https://doi.org/10.1016/j.ijheatmasstransfer.2015.04.112>.
- 1195 71. Adachi JI. *Fluid-driven fracture in permeable rock*. [Ph.D. Thesis]. University of
1196 Minnesota; 2002.
- 1197 72. Adachi J, Detournay E. Self-similar solution of a plane-strain fracture driven by a power-
1198 law fluid. *Int J Numer Anal Methods Geomech.* 2002;26(6):579-604.
1199 <https://doi.org/10.1002/nag.213>.
- 1200 73. Tong S, Mohanty KK. Proppant transport study in fractures with intersections. *Fuel.*
1201 2016;181:463-477. <https://doi.org/10.1016/j.fuel.2016.04.144>.
- 1202
1203